An oncogenic alteration creates a tumor microenvironment that promotes tumor progression by conferring a metabolic advantage to regulatory T cells

Shogo Kumagai[1,2], Yosuke Togashi[1*], Chika Sakai[1], Akihito Kawazoe[3], Masahito Kawazu[4], Toshihide Ueno[4], Eiichi Sato[5], Takeshi Kuwata[6], Takahiro Kinoshita[7], Masami Yamamoto[8], Sachiyo Nomura[9], Tetsuya Tsukamoto[10], Hiroyuki Mano[4], Kohei Shitara[3] and Hiroyoshi Nishikawa[1,2*]

Institutional Affiliations: [1]Division of Cancer Immunology, Research Institute /Exploratory Oncology Research and Clinical Trial Center (EPOC), National Cancer Center, Tokyo/Chiba, Japan, [2]Department of Immunology, Nagoya University Graduate School of Medicine, Nagoya, Japan, [3]Department of Gastrointestinal Oncology, National Cancer Center Hospital East, Chiba, Japan, [4]Division of Cellular Signaling, Group for Cancer Development and Progression, National Cancer Center Research Institute, Tokyo, Japan, [5]Department of Pathology, Institute of Medical Science, Tokyo Medical University, Tokyo, Japan, [6]Department of Pathology and Clinical Laboratories, National Cancer Center Hospital East, Chiba, Japan, [7]Department of Gastric Surgery, National Cancer Center Hospital East, Chiba, Japan, [8]Division of Physiological Pathology, Department of Applied Science, School of Veterinary Nursing and Technology, Nippon Veterinary and Life Science University, Tokyo, Japan, [9]Department of Gastrointestinal Surgery, Graduate School of Medicine, The University of Tokyo, Tokyo, Japan, [10]Department of Pathology, Graduate School of Medicine, Fujita Health University, Aichi Japan.

***Corresponding Authors:**
Hiroyoshi Nishikawa, M.D., Ph.D. (**Lead contact**)
Division of Cancer Immunology, Research Institute/EPOC, National Cancer Center
6-5-1 Kashiwanoha, Kashiwa, Chiba 277-8577, Japan.
Tel: +81-4-7133-1111(ext. 91385 or 2156) / Fax: +81-4-7130-0022
E-mail: hnisihika@ncc.go.jp

Yosuke Togashi, M.D., Ph.D.
Division of Cancer Immunology, Research Institute/EPOC, National Cancer Center
6-5-1 Kashiwanoha, Kashiwa, Chiba 277-8577, Japan.
Tel: +81-4-7133-1111(ext. 2157) / Fax: +81-4-7130-0022
E-mail: ytogashi1584@gmail.com

Manuscript information: text: 50317 characters, summary: 148 words, 7 figures, 7 supplementary figures, 4 supplementary tables.

Summary

Only a small percentage of patients afflicted with gastric cancer (GC) respond to immune checkpoint blockade (ICB). To study the mechanisms underlying this resistance, we examined the immune landscape of GC. A subset of these tumors was characterized by high frequencies of regulatory T (Treg) cells and low numbers of effector T cells. Genomic characterization revealed that these tumors bore mutations in *RHOA* that are known to drive tumorigenesis. *RHOA* mutations in cancer cells increased production of free fatty acids, which are more effectively consumed by Treg cells than by effector T cells, and reduced effector T cell-recruiting chemokines by activating PI3K-AKT signaling pathways. Consequently, *RHOA*-mutated cancers developed a robust immunosuppressive tumor microenvironment (TME) characterized by high Treg cell accumulation despite the noninflamed status. The combination of PI3K-specific blockade and PD-1 blockade improved the immunosuppressive TME and augmented the antitumor effect, overcoming the resistance of *RHOA*-mutated tumors to PD-1 blockade in mouse models. We propose that the metabolic advantage conferred by *RHOA* enables Treg cell accumulation within the tumor, generating an immunosuppressive TME that underlies resistance to ICB.

Introduction

Immune checkpoint blockade (ICB) therapies improve survival of patients with multiple types of cancer, including malignant melanoma, lung cancer, and gastric cancer (GC) (Borghaei et al., 2015; Kang et al., 2017; Reck et al., 2016; Robert et al., 2015; Schachter et al., 2017; Weber et al., 2015). Various immunological facets including PD-ligand 1 (PD-L1) expression in tumor tissues and mutation burden in tumor cells are reportedly associated with clinical responses of ICB (Borghaei et al., 2015; Kang et al., 2017; Reck et al., 2016; Rizvi et al., 2015; Robert et al., 2015; Schachter et al., 2017; Weber et al., 2015). The ratio of $CD8^+$ T cells to regulatory T (Treg) cells in the tumor microenvironment (TME) is also an important factor for prognosis and clinical efficacies (Ayers et al., 2017; Curiel et al., 2004; Sato et al., 2005). In cancer settings, various chemokines that are produced by tumor-infiltrating immune cells have been reported to contribute the migration of immune cells including both effector T cells and suppressive cells into the TME (Fridman et al., 2012; Nagarsheth et al., 2017; Togashi et al., 2019). As Treg cell migration is also dominantly triggered by chemokine networks in the TME, Treg cells are often detected with effector T cells in the inflamed TME (Nagarsheth et al., 2017; Spranger et al., 2013; Togashi et al., 2019). However, some tumors with the noninflamed TME contain abundant Treg cells, suggesting multiple mechanisms of Treg cell expansion in the TME, other than chemokine networks.

As cancer cells mainly consume glucose to fuel aerobic glycolysis for their survival (the Warburg effect), low-glucose and hypoxic conditions that are unfavorable for T cell survival and

functions develop in the TME (Gatenby and Gillies, 2004; Ho and Kaech, 2017; Warburg, 1956). The low-glucose conditions in the TME reportedly contribute to resistance to cancer immunotherapy, via inhibiting the resurgence of effector T cells (Chang et al., 2015). However, it remains unclear why Treg cells are abundant and strongly immunosuppressive in the TME, given the unfavorable conditions for T cells. One plausible explanation is that effector T cells and Treg cells harbor different metabolic profiles for their survival and function (Wang et al., 2017). It has recently been shown that Treg cells require mitochondrial metabolism to maintain immunosuppressive function (Weinberg et al., 2019). However, various issues, such as why some tumors with the noninflamed TME harbor high infiltration of Treg cells without effector T cells, have not fully been addressed.

Considering that the inferior response rate of PD-1 blockade in GC compared to malignant melanoma and lung cancer, GC may establish the rigorous immunosuppressive TME (Borghaei et al., 2015; Kang et al., 2017; Reck et al., 2016; Robert et al., 2015; Schachter et al., 2017; Shitara et al., 2018; Weber et al., 2015). In this study, we therefore aimed at elucidating the immunological landscape in the TME of GC, such as the different frequencies of Treg cells and effector T cells and the immunosuppressive function of Treg cells. Some GC tissue samples exhibited an immunosuppressive TME that was characterized by abundant Treg cells in spite of the noninflamed TME. These tumors harbored *RHOA* gene Y42 mutations, well-known driver mutations in GC (Cancer Genome Atlas Research Network., 2014; Kakiuchi et al., 2014; Wang et al., 2014). We found that the increased production of free fatty acids (FFAs) by GC cells through *RHOA* Y42 mutation signals

contributed to Treg cell accumulation despite the noninflamed TME with low-glucose levels. The combination of PD-1 blockade and an inhibitor of *RHOA* mutation-derived signals overcame resistance of *RHOA*-mutated tumors to PD-1 blockade in mouse models, proposing a potential combination cancer immunotherapy.

Results

Patients with *RHOA* Y42 mutations have an immunosuppressive TME characterized by Treg cell accumulation regardless of the noninflamed status of the TME.

We first analyzed the immunological status (inflamed or noninflamed) and cell types in tumor samples from 23 GC patients who had undergone surgical resection (**Table S1**). According to immune-related gene expression evaluated by RNA sequencing (RNA-seq), eight tumor samples had a noninflamed TME, and the remaining tumor samples had an inflamed TME (**Figure 1A**). In addition to RNA-seq, whole-exome sequencing (WES) was performed with the same samples and showed no correlation between the immunological status of the tumors (inflamed or noninflamed) and tumor mutational burden (TMB), which is reportedly important for antitumor immunity (Rizvi et al., 2015; Rooney et al., 2015) (**Figure 1A**).

To precisely evaluate Treg cells in the TME, given the transient upregulation of FOXP3 expression upon T cell receptor (TCR) stimulation in naive T cells (Tran et al., 2007), tumor-infiltrating lymphocytes (TILs) were subjected to flow cytometry (FCM) and assessed with our classification dividing human $FOXP3^{+}CD4^{+}$ cells into three subpopulations based on the expression levels of the naive cell marker CD45RA and FOXP3 (Miyara et al., 2009; Saito et al., 2016; Togashi et al., 2019): naive Treg cells [Fraction (Fr.) I: nTreg cells, $CD45RA^{+}FOXP3^{low}CD4^{+}$] with weak immunosuppressive function; effector Treg cells (Fr. II: eTreg cells, $CD45RA^{-}FOXP3^{high}CD4^{+}$) with strong immunosuppressive function; and non-Treg cells (Fr. III: $CD45RA^{-}FOXP3^{low}CD4^{+}$) without

immunosuppressive function (**Figure S1A and S1B**). From the FCM and RNA-seq data, four patients bore an immunosuppressive TME that was characterized by Treg cell accumulation regardless of the noninflamed status of the TME (**Figure 1A**), although Treg cells are generally accompanied by effector T cell infiltration in the inflamed TME (Spranger et al., 2013). The WES analysis revealed that two of these patients possessed the *RHOA* Y42C mutation. Accordingly, GC patients with *RHOA* Y42C (*RHOA* Y42C-GCs) harboring a low TMB exhibited lower expression of immune-related genes, including *CD8A*, *IFNG*, and *CD274*, than GC patients lacking the mutation (**Figure S1C and S1D**). The frequency of tumor-infiltrating eTreg cells, the ratio of tumor-infiltrating eTreg cells/$CD8^+$ T cells, and the expression of CTLA-4, a key molecule in Treg cell-mediated immunosuppression (Wing et al., 2008), by tumor-infiltrating eTreg cells tended to be higher in *RHOA* Y42C-GCs than in *RHOA* wild-type (WT) GCs (**Figure S1A, S1B, S1E and S1F**). To validate the immunosuppressive TME of GCs with the *RHOA* mutations, eighty-five advanced GC patients' samples from another cohort were analyzed (**Table S2**). *RHOA* Y42C or Y42S mutation was detected in seven (five or two, respectively) GC samples with digital polymerase chain reaction (PCR). The frequency of eTreg cells, the ratio of eTreg cells/$CD8^+$ T cells, and the expression of CTLA-4 by eTreg cells in the TME were significantly higher in *RHOA* Y42 mutated-GCs than in *RHOA* WT-GCs (**Figure 1B-1E**). Significantly lower expression of *CD8A* and higher expression of *FOXP3* in *RHOA* mutated-GCs than *RHOA* WT-GCs were detected with real-time quantitative reverse transcription PCR (qRT-PCR) (**Figure 1F**). Higher eTreg cell infiltration was also observed with immunohistochemistry (IHC) (**Figure 1G and S1G**).

The analysis of the Cancer Genome Atlas (TCGA) data confirmed the significantly higher expression of *FOXP3* and higher ratio of *FOXP3*/*CD8A* expression in *RHOA* Y42 mutated-GCs compared with *RHOA* WT-GCs (Cancer Genome Atlas Research Network., 2014) (**Figure S1H**). These findings suggest that activated eTreg cells accumulate in the TME in spite of the noninflamed phenotype in *RHOA* mutated-GCs.

RHOA Y42C reduces effector T cell-recruiting chemokine production by increasing the activity of the PI3K-AKT signaling pathways.

To explore how the noninflamed TME was developed by *RHOA* Y42 mutations, comprehensive gene expression was examined with microarray analyses using *RHOA* WT or Y42C-overexpressing human GC cell lines (MKN1^{WT}, MKN1^{Y42C}, MKN45^{WT}, and MKN45^{Y42C}) and murine gastrointestinal cell lines (MC-38^{WT}, MC-38^{Y42C}, CT26-NY-ESO-1^{WT}, and CT26-NY-ESO-1^{Y42C}) (**Figure 2A**). When we focused on cytokine or chemokine gene expression, the expression of *CXCL10* and *CXCL11*, which recruit effector CD8^{+} T cells (Gorbachev et al., 2007; Griffith et al., 2014; Hensbergen et al., 2005; Van Raemdonck et al., 2015; Zumwalt et al., 2015), was lower in MKN1^{Y42C} cells than in MKN1^{WT} cells (**Figure 2B**). In addition, differential analyses of transcription factor expression between MKN1^{WT} and MKN1^{Y42C} cells uncovered the concurrent reduction in the expression of *IRF1*, which reportedly regulates *CXCL10* and *CXCL11* (Harikumar et al., 2014; Yang et al., 2007) (**Figure 2B**). Real-time qRT-PCR, enzyme-linked immunosorbent assay (ELISA), and western blotting analyses

confirmed the simultaneous reduction in IRF1 expression and CXCL10 and CXCL11 expression in the *RHOA* Y42C-overexpressing GC cell lines (**Figure 2C-2G**). Furthermore, similar trends were observed in gene expression of clinical GC samples (**Figure 2H and Figure S1I**). Overall, the *RHOA* Y42 mutations decrease the levels of effector T cell-recruiting chemokines such as CXCL10 and CXCL11 via the reduction of IRF1 expression.

Gene alterations in the effector domain of *RHOA,* including Y42C, impair binding to effector proteins, thereby decaying the signaling pathways of RHOA (Bae et al., 1998; Sahai et al., 1998; Wang et al., 2014). Accordingly, *RHOA* Y42C cells markedly reduced the amount of the GTP-associated form detected by Rhotekin-Rho binding domain pulldown assays, which was recovered by overexpression of *RHOA* WT (**Figure 2A**). This reduction decreased phosphorylation of PTEN and increased phosphorylation of AKT, suggesting a defect in the RHOA/ROCK/PTEN signaling pathways (**Figure 2F**). Phosphorylated GSK3β, which is induced by the PI3K-AKT signaling pathways, reportedly suppresses STAT1 (Tsai et al., 2009), a well-known transcription factor of IRF1 (Ramana et al., 2000). In line with this, the increased phosphorylated GSK3β level induced by *RHOA* Y42C led to the suppression of STAT1, resulting in IRF1 expression reduction (**Figure 2F and 2G**). Therefore, *RHOA* Y42C reduces the expression of *CXCL10* and *CXCL11* by upregulating the PI3K-AKT signaling pathways (**Figure S2A**).

***RHOA* Y42C-GCs with high eTreg cell infiltration in the TME efficiently produce FFAs via**

PI3K-AKT/mTOR signaling pathways.

The protein expression of CCL1, CCL17, and CCL22, which reportedly recruit eTreg cells (Curiel et al., 2004; Hoelzinger et al., 2010; Mantovani et al., 2017; Togashi et al., 2019), by MKN1^{Y42C} and MKN1^{WT} cells showed a comparable expression regardless of *RHOA* gene status (**Figure 2I**). Rather a trend in lower expression of *CCL1*, *CCL17,* and *CCL22* in *RHOA* Y42 mutated-GCs compared with *RHOA* WT-GCs was observed (**Figure 2H and Figure S1I**), suggesting that other mechanism(s) may be mainly involved in eTreg cell accumulation and immunosuppression in the TME of *RHOA* Y42 mutated-GCs.

To elucidate the mechanism(s) of eTreg cell accumulation and immunosuppression by *RHOA* Y42 mutations, we employed Gene Set Enrichment Analysis (GSEA) of the RNA-seq, which revealed that the gene set related to fatty acid metabolism was significantly enriched in *RHOA* Y42C-GCs (**Figure 3A**). Consistently, the expression of *FASN* (encoding FAS), which plays an important role in fatty acid synthesis (Wakil, 1989), was significantly higher in *RHOA* Y42 mutated-GCs than in *RHOA* WT-GCs (**Figure 3B and Figure S1I**). eTreg cells possess a different metabolic profile compared with effector T cells which preferentially utilize glucose: Treg cells depend on lipid oxidation for their survival (Michalek et al., 2011). Cancer cells deprive glucose from the TME and produce fatty acids through *de novo* synthesis from glucose (the Warburg effect) (Currie et al., 2013; Rohrig and Schulze, 2016), resulting in lower glucose concentration in the TME than in the periphery (**Figure S3A**). Tumor-infiltrating Treg cells take up more FFAs than other T cell subsets (Muroski et al., 2017). Therefore,

we hypothesized that *RHOA* Y42 mutated-GCs produced larger amounts of FFAs via increased FAS expression, which contributed to the prolonged survival of eTreg cell subset in the TME compared with that of other effector T cell subsets. In line with this hypothesis, both *FASN* mRNA and FAS protein expression was significantly higher in *RHOA* Y42C-overexpressing cell lines than in *RHOA* WT-overexpressing cell lines (**Figure 3C-3E**). The activation of PI3K-AKT/mTOR/S6K signaling pathways reportedly elevates FAS expression via transcription factor SREBP-1 (Duvel et al., 2010; Peterson et al., 2011; Porstmann et al., 2008). We then examined these signaling pathways using the cell lines, and the elevations in these signaling pathways in the *RHOA* Y42C-overexpressing cell lines were observed by western blotting (**Figure 3D**). Accordingly, the total concentration of FFAs in the culture was significantly higher in the *RHOA* Y42C-overexpressing cell line culture than in the *RHOA* WT-overexpressing cell line culture (**Figure 3F**). In addition, liquid chromatography-mass spectrometry (LC-MS) confirmed the higher concentration of FFA species in the culture of MKN1^{Y42C} cells than in that of MKN1^{WT} cells (**Figure 3F**). Furthermore, we assessed the differences in the total content of FFAs of tumors between *RHOA* WT-overexpressing tumors and *RHOA* Y42C-overexpressing tumors. MC-38^{Y42C} and CT26-NY-ESO-1^{Y42C} tumors also harbored larger amounts of FFAs compared with the corresponding wild-type cells *in vivo* (**Figure3G**). These results indicate that *RHOA* Y42C further increases FFA production via the activation of PI3K-AKT/mTOR/S6K signaling pathways compared with *RHOA* WT (**Figure S2B**).

Higher FFA concentration in a low-glucose condition increases Treg cells.

The higher FFA production by *RHOA* Y42C cancer cells prompted us to explore whether the abundant FFAs in the TME contributed to the prolonged survival of Treg cells. To this end, we employed a low-glucose medium supplemented with increasing concentrations of palmitate to culture peripheral blood mononuclear cells (PBMCs) from healthy individuals. In a concentration-dependent manner, the frequency of eTreg cells increased, resulting in a higher ratio of eTreg cells/$CD8^+$ T cells (**Figure 3H**). To further confirm the dominant Treg cell expansion compared with other T cell subsets, we sorted $CD8^+$ T cells, $CD45RA^-CD25^-CD4^+$ T cells (conventional $CD4^+$ T cells; conv $CD4^+$ T cells) and $CD45RA^-CD25^{high}CD4^+$ T cells (eTreg cells) from PBMCs and each T cell subset was separately cultured to evaluate the proliferation and apoptosis in the titrated concentrations of FFAs (palmitate or oleate) (**Figure S3B-S3H**). eTreg cells were more proliferative and less apoptotic compared with other T cell subsets in response to increasing concentration of FFAs under a low-glucose condition, while every T cell subset consumed FFAs under a low-glucose condition (**Figure S3B-S3H**). In addition, eTreg cells exhibited a stronger suppressive activity in an FFA concentration-dependent manner in a low-glucose condition (**Figure S3I and S3J**).

We next addressed the differences in fatty acid metabolism among T cell subsets *in vivo* using the murine MC-38 cell line. Lipid uptake and content, which were assessed with BODIPY FL C16 and 493, respectively, were significantly higher in $Foxp3^+CD4^+$ cells (Treg cells) than in $Foxp3^-CD4^+$ T cells or $CD8^+$ T cells in the TME (**Figure 4A and 4B**). Additionally, the expression of molecules

related to FFA uptake and metabolism, including CD36 (a scavenger receptor mediating the uptake of FFAs), CPT1A (the rate-limiting enzyme in long-chain fatty acid oxidation), PPARα, and PPARγ in Treg cells was significantly higher than that in Foxp3$^-$CD4$^+$ T cells or CD8$^+$ T cells (**Figure 4C-4E**). In accordance with the animal model data, TILs from GC patients (see **Table S3** for patient characteristics**)** showed higher lipid uptake and content in eTreg cells than in Foxp3$^-$CD4$^+$ T cells or CD8$^+$ T cells (**Figure 4F and 4G**). The differences in glucose uptake among T cell subsets in the TME were also examined. Compared with Treg cells, CD8$^+$ T cells exhibited increased glucose uptake (assessed with 2-NBDG) accompanied by higher expression of GLUT1 (**Figure 4H and 4I**). Overall, Treg cells effectively utilize FFAs for their survival compared with the other T cell subsets in the TME, whereas conventional CD4$^+$ T cells and CD8$^+$ T cells are likely to depend on glucose consumption.

To validate the importance of this metabolic change for Treg cells, we investigated the effects of FFAs on tumor-infiltrating lymphocytes using *Fasn*-overexpressing MC-38 murine cell line (MC-38^{Fasn}) that produced FFAs (**Figure 4J and 4K**). The frequency and the number (counts/tumor weight) of Treg cells, and the ratio of Treg cells/CD8$^+$ T cells in the TME were significantly higher in MC-38^{Fasn} tumors than in MC-38^{mock} tumors (**Figure 4L-4N**). CTLA-4 expression by Treg cells in the TME was significantly higher in the MC-38^{Fasn} tumors than in the MC-38^{mock} tumors (**Figure 4O and 4P**), suggesting the importance of FFAs for the survival and immunosuppressive function of Treg cells. Additionally, antitumor effects with anti-PD-1 monoclonal antibody (mAb) observed in MC-38^{mock} tumors were significantly dampened in MC-38^{Fasn} tumors (**Figure 4Q**). Taken together, higher

amounts of FFAs in the TME not only contribute to the better survival and immunosuppressive function of Treg cells, but also weaken the antitumor efficacy of anti-PD-1 mAb.

***RHOA* Y42C develops an immunosuppressive TME *in vitro* and *in vivo*.**

We further explored the critical role of FFAs for the better survival and immunosuppressive function of Treg cells in *RHOA* Y42-mutated tumors. Sorted eTreg cells, conv $CD4^+$ T cells or $CD8^+$ T cells were cultured with the supernatants from $MKN1^{WT}$ or $MKN1^{Y42C}$ cells to examine the proliferation and apoptosis of each T cell subset (**Figure S2C-S2G**). eTreg cells were significantly more proliferative and less apoptotic than other T cell subsets, thereby the number of eTreg cells was significantly higher in the cultures with supernatants from $MKN1^{Y42C}$ than in those from $MKN1^{WT}$ (**Figure S2C-S2G**).

To assess the immunological effect of *RHOA* Y42C on the TME of GCs in addition to MC-38, we established *RHOA* WT- or *RHOA* Y42C-overexpressing YTN16; a murine gastric adenocarcinoma cell line. The frequency and the number of Treg cells and the ratio of Treg cells/$CD8^+$ T cells were significantly higher in *RHOA* Y42C-overexpressing tumors than in *RHOA* WT-overexpressing tumors, whereas the numbers of $CD8^+$ T cells and conv $CD4^+$ T cells were significantly lower (**Figure 5A-5C**). The abundant Treg cells in the TME of *RHOA* Y42C-overexpressing tumors were due to a less apoptotic and more proliferative nature compared with *RHOA* WT-overexpressing tumors (**Figure S2H-S2M**). In addition, Treg cells took in a larger amount of FFAs, and the expression

of molecules related to FFA uptake and metabolism by tumor-infiltrating Treg cells was higher in *RHOA* Y42C-overexpressing tumors than in *RHOA* WT-overexpressing tumors (**Figure 5D-5G**).

We next examined the immunological phenotypes of Treg cells in the TME. The expression of activation markers by Treg cells in the TME was significantly higher in the MC-38^{Y42C} tumors than in the MC-38WT tumors in accordance with human GC with *RHOA* Y42 mutated-GCs (**Figure 1D, 1E, 5H and 5I and Figure S1E and S1F**). Antigen-presenting cells (APCs) are an important target of Treg cells, as previously reported (Maeda et al., 2014; Qureshi et al., 2011; Wing et al., 2008). The expression of CD80 and CD86 by APCs in the TME was decreased in the MC-38^{Y42C} tumors (**Figure 5J and 5K**). Overall, abundant FFAs in the TME of tumors with *RHOA* Y42C contribute to compelling not only the survival but also the immunosuppressive function of Treg cells.

Tumors with *RHOA* Y42C are resistant to PD-1 blockade treatment, which can be overcome by combination with a PI3Kβ inhibitor.

Tumor growth was comparable between *RHOA* WT- and *RHOA* Y42C-overexpressing tumors in immunocompetent and immunocompromised mice, while differences in immunological phenotypes of TILs were detected according to the alteration of the *RHOA* gene (**Figure S4A-S4C**). We then addressed the antitumor efficacy of anti-PD-1 mAb *in vivo*. Anti-PD-1 mAb failed to inhibit the growth of *RHOA* Y42C-overexpressing tumors compared with that of *RHOA* WT-overexpressing tumors (**Figure 6A and Figure S4D, S5A, and S5B**). The frequencies of MuLV-15E tetramer^{+}, CD62L^{-}CD44^{+},

TNF-α^+IFN-γ^+, $CD69^+$ and Granzyme B^+ tumor-infiltrating $CD8^+$ T cells were increased by anti-PD-1 mAb in MC-38^{WT} tumors, but not in MC-38^{Y42C} tumors (**Figure 6B and 6C and Figure S4E-S4L**).

To elucidate the importance of abundant FFAs in the TME derived from the *RHOA* Y42C in the resistance to PD-1 blockade, we addressed whether *Fasn* knock-down or CD36 blockade recovered the antitumor efficacy of anti-PD-1 mAb in *RHOA* Y42C-overexpressing tumors. Treg cells, in addition to their CTLA-4 expression, were significantly decreased in *Fasn* knocked-down MC-38^{Y42C} tumors in number, while $Foxp3^-CD4^+$ T cells and $CD8^+$ T cells were significantly increased (**Figure 6D-6J**). Accordingly, the tumor growth of *Fasn* knocked-down MC-38^{Y42C} was significantly inhibited by anti-PD-1 mAb (**Figure 6K and Figure S4M**). We next performed CD36 blockade to inhibit FFA transport. Anti-CD36 mAb significantly decreased the number of Treg cells, as well as their CTLA-4 expression in MC-38^{Y42C} tumors, leading to the increase in $Foxp3^-CD4^+$ T cells and $CD8^+$ T cells (**Figure 6L-6P**). The antitumor efficacy of anti-PD-1 mAb was also significantly improved by the combination with CD36 blockade (**Figure 6Q and Figure S5C and S5D**). Together with the data of *Fasn*-overexpressing MC-38 cell line **(Figure 4Q)**, abundant FFAs in the TME derived from *RHOA* Y42C inhibit the antitumor efficacy of anti-PD-1 mAb.

We then hypothesized that inhibiting PI3K-AKT signaling pathways in *RHOA* Y42C-overexpressing tumors could overcome the resistance to anti-PD-1 mAb treatment because PI3K-AKT signaling pathways play important roles in this immunosuppressive TME developed by *RHOA* Y42C. While the inhibition of PI3K-AKT signaling pathways may influence the viabilities of immune cells

(Fruman et al., 2017), the PI3Kβ isoform can regulate PI3K-AKT signaling pathways in tumors with PTEN deficiency without directly affecting Treg cell development, maintenance or proliferation (Jia et al., 2008; Sauer et al., 2008). We then employed a selective PI3Kβ small-molecule inhibitor, GSK2636771, to address whether modulating PI3K-AKT signaling pathways could overcome the immunosuppressive phenotype. GSK2636771 inhibited AKT phosphorylation in a concentration-dependent manner, mainly in *RHOA* Y42C-overexpressing cancer cells, resulting in increased IRF1, CXCL10 and CXCL11 expression and decreased FAS expression *in vitro* (**Figure S6A-S6D**). Additionally, GSK2636771 significantly reduced total FFA production from *RHOA* Y42C-overexpressing cancer cells (**Figure S6E and S6F**). Moreover, GSK2636771 decreased Treg cells and increased $CD8^+$ T cells in the TME of MC-38^{Y42C} tumors (**Figure 7A-7C**). The expression of activation markers on Treg cells was decreased (**Figure 7D and 7E**). The maturation of tumor-infiltrating APCs was significantly improved by GSK2636771 (**Figure 7F and 7G**).

Next, the antitumor efficacy of anti-PD-1 mAb combined with GSK2636771 was examined. Each monotherapy hardly inhibited tumor growth, but combined treatment with GSK2636771 and anti-PD-1 mAb significantly delayed MC-38^{Y42C} tumor growth and activated tumor-infiltrating $CD8^+$ T cells (**Figure 7H-7J and Figure S5E and S5F**). In contrast to the MC-38^{Y42C} tumors, MC-38^{WT} tumors showed no significant immunological changes in the TME by GSK2636771, resulting in no combination efficacy (**Figure S7I-S7O**). Given the importance of controlling Treg cells in the TME, we assessed whether anti-CTLA-4 mAb, that is well known to control Treg cells (Selby et al., 2013;

Simpson et al., 2013; Wing et al., 2008), augmented the efficacy of anti-PD-1 mAb in MC-38^{Y42C} tumors. The combination treatment significantly slowed the tumor growth compared with single mAb treatment (**Figure 7K and Figure S5G and S5H**). We propose that tumors with *RHOA* Y42C are resistant to PD-1 blockade as a monotherapy due to the immunosuppressive TME, which can be overcome by the combination with a PI3Kβ inhibitor or Treg cell-targeted treatment such as anti-CTLA-4 mAb.

GC patients with *RHOA* Y42 mutations fail to respond to PD-1 blockade therapy.

Finally, we evaluated the efficacy of anti-PD-1 mAb in three advanced GC patients with *RHOA* Y42 mutations (**Table S4**) and revealed that no patient responded to anti-PD-1 mAb. In particular, one patient experienced progressive disease after one course of anti-PD-1 mAb therapy (**Figure S4N**).

Discussion

In this study, we revealed that a subset of GC exhibited an immunosuppressive TME that was characterized the accumulation of Treg cells in the absence of other inflammatory features. Some of these tumors harbored mutations in *RHOA*, including *RHOA* Y42C, which is one of the famous driver mutations in GCs and account for 10% to 25% of diffuse-type GCs (Cancer Genome Atlas Research Network., 2014; Kakiuchi et al., 2014; Wang et al., 2014). *RHOA* mutated-GCs harbored a low TMB and inhibited effector T cell infiltration into the TME by decreasing IRF1 expression through PI3K-AKT signaling pathways, resulting in decreased production of the effector T cell-recruiting chemokines CXCL10 and CXCL11. On the other hand, higher tumor infiltration of Treg cells was not strongly correlated with the expression of Treg cell-recruiting chemokines; rather, the *RHOA* mutation induced abundant FFA production via the PI3K-AKT signaling pathways. This metabolic profile resulted in enhanced eTreg cell survival and immunosuppressive function in an FFA dose-dependent manner since Treg cells rely on mitochondrial metabolism to maintain immunoregulatory gene expression and immunosuppressive function, while effector T cells rely on a different metabolic profile (Angelin et al., 2017; Wang et al., 2017).

We demonstrated an immunological influence of *RHOA* Y42C on inhibiting $CD8^+$ T cell infiltration by changing the chemokine milieu in the TME via activating PI3K-AKT signaling pathways. Similar immunological influence has been reported in tumors harboring alterations in FAK, PTEN, EGFR, and WNT-β-catenin that all showed poor responses to immune checkpoint blockade

(ICB) therapy (Jiang et al., 2016; Peng et al., 2016; Spranger et al., 2015). Particularly, activating PI3K-AKT signaling pathways are involved in *EGFR* mutations (Sugiyama et al., 2020) and *PTEN* loss (Peng et al., 2016). In fact, we found that *RHOA* Y42 mutated-GCs exhibited a limited clinical response to PD-1 blockade therapies, while PD-1 blockade therapies demonstrate clinical efficacy in unresectable advanced or recurrent GCs with response rates of 10-25% (Kang et al., 2017). In line with this, diffuse-type GCs, as which *RHOA* mutated-GCs are basically classified, are resistant to PD-1 blockade therapies (Kang et al., 2017). Therefore, our data can be applied for stratifying patients eligible for PD-1 blockade therapies via excluding a plausible non-responder population, leading to the improvement in response rates of ICB in GCs. In addition, Treg cell infiltration can be reportedly related to hyperprogressive disease by PD-1 blockade therapies (Kamada et al., 2019), further suggesting that *RHOA* mutated-GCs are not good candidates for PD-1 blockade monotherapy. Other types of malignancies with *RHOA* mutations that enhance PI3K-AKT signaling pathways may also provide the similar immunosuppressive effect (Yoo et al., 2014).

Various types of PI3K inhibitors have been tested in clinical trials involving patients with a wide range of cancers (Janku et al., 2018). Among these inhibitors, PI3Kδ inhibitors have been approved for clinical application by the U.S. Food and Drug Administration (FDA) (Janku et al., 2018), but the inactivation of p110δ in T cells may impair the differentiation of effector $CD4^+$ T cells (Okkenhaug et al., 2006; Soond et al., 2010) and $CD8^+$ T cells (Macintyre et al., 2011) as well as the functions of Treg cells (Ali et al., 2014; Patton et al., 2006). In contrast, treatment with a PI3Kβ inhibitor provides little

impact on immune cells (Peng et al., 2016). We employed a PI3Kβ inhibitor to inhibit PI3K-AKT signaling pathways activated by *RHOA* Y42C in combination with ICB, leading to a far stronger antitumor effect than that produced by ICB alone. Thus, the PI3Kβ inhibitor could become a promising combination therapy with ICB in *RHOA* mutated-malignancies and other types of gene alterations activating PI3K-AKT signaling pathways.

Foxp3 expression is involved in various metabolic programs, and $Foxp3^+$ Treg cells maintain high levels of AMPK activation, contributing to the high reliance on lipid oxidation (Angelin et al., 2017; Gerriets et al., 2016; Michalek et al., 2011; Muroski et al., 2017). Abundant FFA production by PI3K-AKT-mTOR signaling pathways provided a metabolic advantage for the survival and immunosuppressive function of Treg cells. The higher concentration of FFAs in the TME in *RHOA* Y42 mutated-GCs enhanced survival and immunosuppressive function of Treg cells even in low-glucose environments. Additionally, a similar TME with abundant FFAs is reported in *Kras*-mutated cancers (Gouw et al., 2017), suggesting that the mechanism of metabolic advantage by driver gene mutations observed in our study may be a common system for developing an immunosuppressive TME. The glucose deprivation in the TME, which is lethal to $CD8^+$ T cells and $FOXP3^-CD4^+$ T cells, may have minimal influences on eTreg cells. Yet, it has not been determined whether fatty acid production by cancer cells is sufficient for Treg cell survival and immunosuppressive function, while increased fatty acid production in cancer cells may increase lipid availability in the TME (Rohrig and Schulze, 2016). We showed that eTreg cells could take in larger amount of FFAs provided by the *RHOA*-mutated

tumors and more effectively employ lipid metabolism pathways for their survival and immunosuppressive functions than could other T cell subsets in the TME. This means that FFA doses in the TME can reflect the survival and immunosuppressive function of Treg cells. Nevertheless, some reports show a crucial role for aerobic glycolysis in Treg cells, as observed in effector T cells (Fan and Turka, 2018; Gerriets et al., 2016; Kishore et al., 2017; Li et al., 2019; Procaccini et al., 2016). These contradictory findings may be partially due to anatomical location. Indeed, tissue-resident Treg cells that localize in nonlymphoid tissues, such as the visceral adipose tissue, are highly dependent on lipid metabolism (Cipolletta et al., 2012). Treg cells therefore have a more redundant metabolic profile than other T cell subsets and can survive and function even in low-glucose and hypoxic conditions like TMEs.

In conclusion, we show that *RHOA* mutations establish an immunosuppressive TME characterized by eTreg cell infiltration regardless of the non-inflammatory TME in humans. The immunosuppressive microenvironment of *RHOA* Y42 mutated-GCs is induced by reduced levels of effector T cell-recruiting chemokines and increased production of FFAs via the activation of PI3K-AKT signaling pathways: eTreg cells survive and function with FFA metabolism, while glucose deprivation is lethal to $CD8^+$ T cells and conventional $CD4^+$ T cells. We thus propose that driver gene alterations are essential not only in the proliferation and survival of cancer cells but also in the development of an immune escape-enabling TME, warranting further evaluation of cancer immunotherapies combined with molecular-targeted therapies against driver gene alterations.

Acknowledgments

We thank Drs. Kota Itahashi, Takuma Irie, Eri Sugiyama, Ms. Tomoka Takaku, Miyuki Nakai, Konomi Onagawa, Megumi Takemura, Chie Haijima, Megumi Hoshino, Kumiko Yoshida, Yumi Osada and Miho Ozawa for their technical assistance.

Funding Sources: This study was supported by Grants-in-Aid for Scientific Research [S grant no. 17H06162 (H.N.), Challenging Exploratory Research Grant no. 16K15551 (H.N.), Young Scientists no. 17J09900 (Y.T.), and JSPS Research Fellowship no. 18J21551 (S.K.)] from the Ministry of Education, Culture, Sports, Science and Technology of Japan; by the Projects for Cancer Research by Therapeutic Evolution [P-CREATE, no. 16cm0106301h0001 (H.N.), no. 16cm0106301h0001 (H.M.), no. 18cm0106502s0403 (M.K.) and no. 18cm0106340h0001 (Y.T.)], by the Development of Technology for Patient Stratification Biomarker Discovery grant [no.19ae0101074s0401 (H.N.)], and by Leading Advanced Projects for Medical Innovation [LEAP, no. 18am0001001h9905 (H.M.)] from the Japan Agency for Medical Research and Development (AMED); by the National Cancer Center Research and Development Fund [no. 28-A-7 and 31-A-7 (H.N.)]; by the Naito Foundation (Y.T. and H.N.); by the Takeda Science Foundation (Y.T.); by the Kobayashi Foundation for Cancer Research (Y.T.); by the Novartis Research Grant (Y.T.); by the Bristol-Myers Squibb Research Grant (Y.T.), and by the SGH Foundation (Y.T.). This study was executed in part as a research program supported by Ono Pharmaceutical.

Author contributions

Conceptualization, Y.T., K.S., and H.N.; Methodology, S.K., Y.T., and H.N.; Investigation, S.K., C.S., A.K., M.K., T.U., E.S., M.Y., S.N., T.T., and T.K.; Writing-Original Draft, Review, and Editing, S.K., Y.T., T.K., H.M., K.S., and H.N.; and Funding Acquisition, S.K., Y.T., M.K., H.M., and H.N.

Declaration of interests

Y.T. has received honoraria from Bristol-Myers Squibb, Ono Pharmaceutical, Chugai Pharmaceutical, Boehringer Ingelheim GmbH, MSD, and AstraZeneca and has received research funding from KOTAI biotechnologies outside of this work. T.K. has received research funding from Ono Pharmaceutical and has received honoraria from Chugai Pharmaceutical outside of this work. H.M. has served as a member of the scientific advisory board for Chugai Pharmaceutical and has received research funding from Ono Pharmaceutical outside of this work. K.S. has served as a member of the scientific advisory board for Ono Pharmaceutical, Eli Lilly, Bristol-Myers Squibb, Astellas Pharmaceutical, Takeda Pharmaceutical, and Pfizer; has received research funding from Ono Pharmaceutical, Eli Lilly, Sumitomo Dainippon Pharmaceutical, Daiichi-Sankyo, Taiho Pharmaceutical, Chugai Pharmaceutical, and MSD; and has received honoraria from Novartis Pharma, AbbVie GK and Yakult Pharmaceutical Industry outside of this work. H.N. received research funding from Ono Pharmaceutical for this work, honoraria and research funding from Chugai Pharmaceutical and Bristol-Myers Squibb, honoraria

from Ono Pharmaceutical and MSD, and research funding from Taiho Pharmaceutical, Daiichi-Sankyo, Kyowa Kirin, Zenyaku Kogyo, Oncolys BioPharma, Debiopharma, Asahi-Kasei, Astellas Pharmaceutical, Sumitomo Dainippon Pharmaceutical, Sysmex, and BD Japan outside this study. All the other authors declare that they have no competing financial interests.

Figure

Figure 1. *RHOA* Y42 mutated-GCs harbor high eTreg cell infiltration regardless of the noninflamed status of the TME.

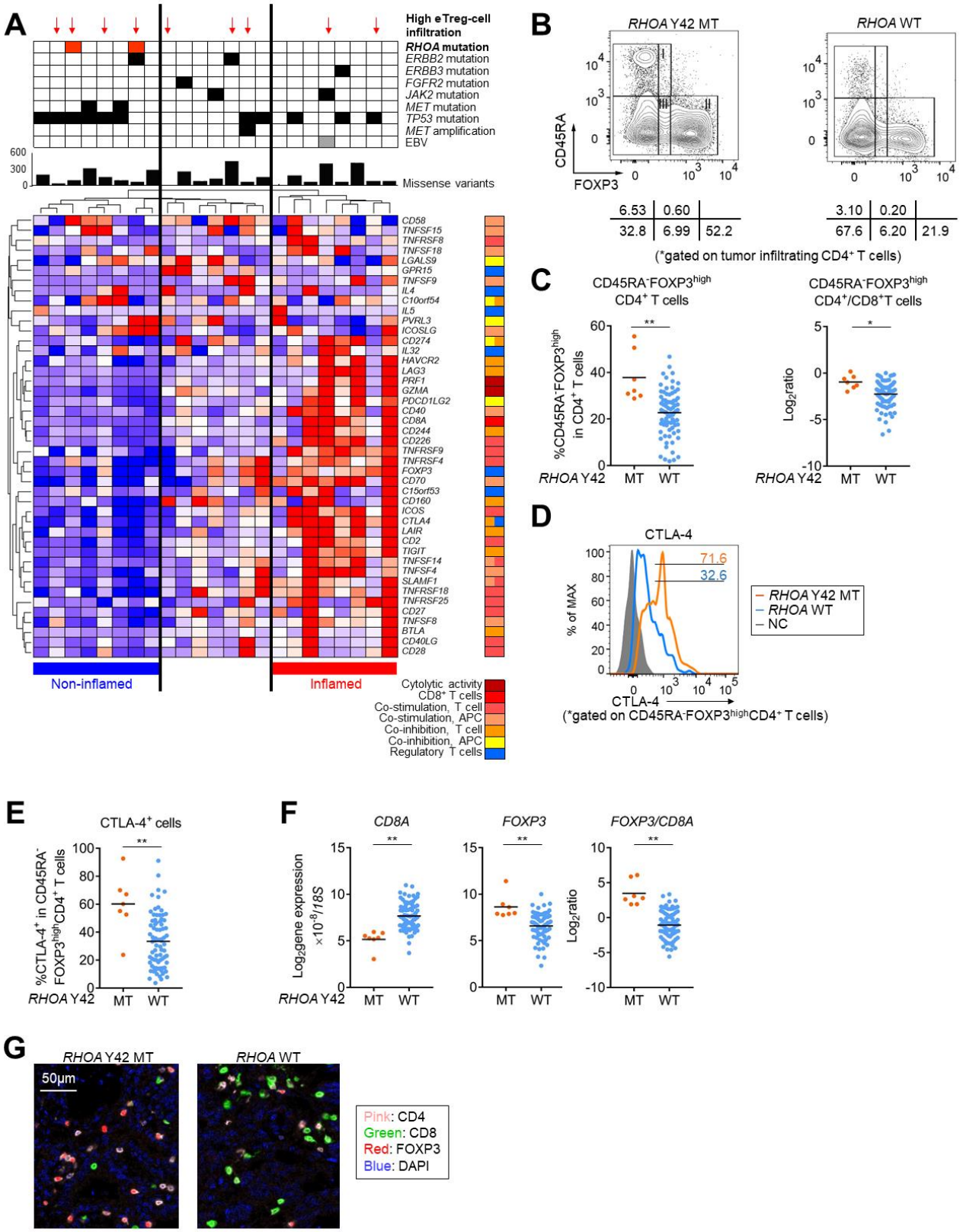

(A) RNA from twenty-three GC samples was subjected to RNA-seq and clustered by immune-related gene sets ($CD4^+$ Treg cells, $CD8^+$ T cell, co-stimulation APC and T cell, co-inhibition APC and T cell, and cytolytic activity). WES was performed with the same tumors. Representative driver gene alterations (filled sections) and the number of missense variants (bars) are shown. Red arrows indicate samples where the tumor-infiltrating eTreg cell proportion in the $CD4^+$ T cell population is >20%. Red, *RHOA* Y42C; black, other representative driver gene alterations; and gray, EBV. **(B and C)** Representative contour plots of eTreg cells in eighty-five advanced GC samples classified according to *RHOA* gene status (**B**) and summaries (**C**) are shown. TILs from tumor tissue samples were subjected to FCM. I, fraction I (naive Treg cells); II, fraction II (eTreg cells); III, fraction III (non-Treg cells). **(D and E)** Representative histogram plots of CTLA-4 expression by eTreg cells in advanced GC samples classified according to *RHOA* gene status **(D)** and summary **(E)** are shown. TILs from tumor tissue samples were subjected to FCM. (**F**) *CD8A* and *FOXP3* expression (left and middle) and the ratio of *FOXP3* to *CD8A* expression (right) in advanced GC samples according to *RHOA* gene status was examined by real-time qRT-PCR. **(G)** Representative pictures of multiplexed IHC for CD4 (pink), CD8 (green), FOXP3 (red) and DAPI (blue). MT, mutation; WT, wild-type; NC, negative control.

Figure 2. *RHOA* Y42C reduces CXCL10, CXCL11, and IRF1 expression via the activation of PI3K-AKT signaling pathways.

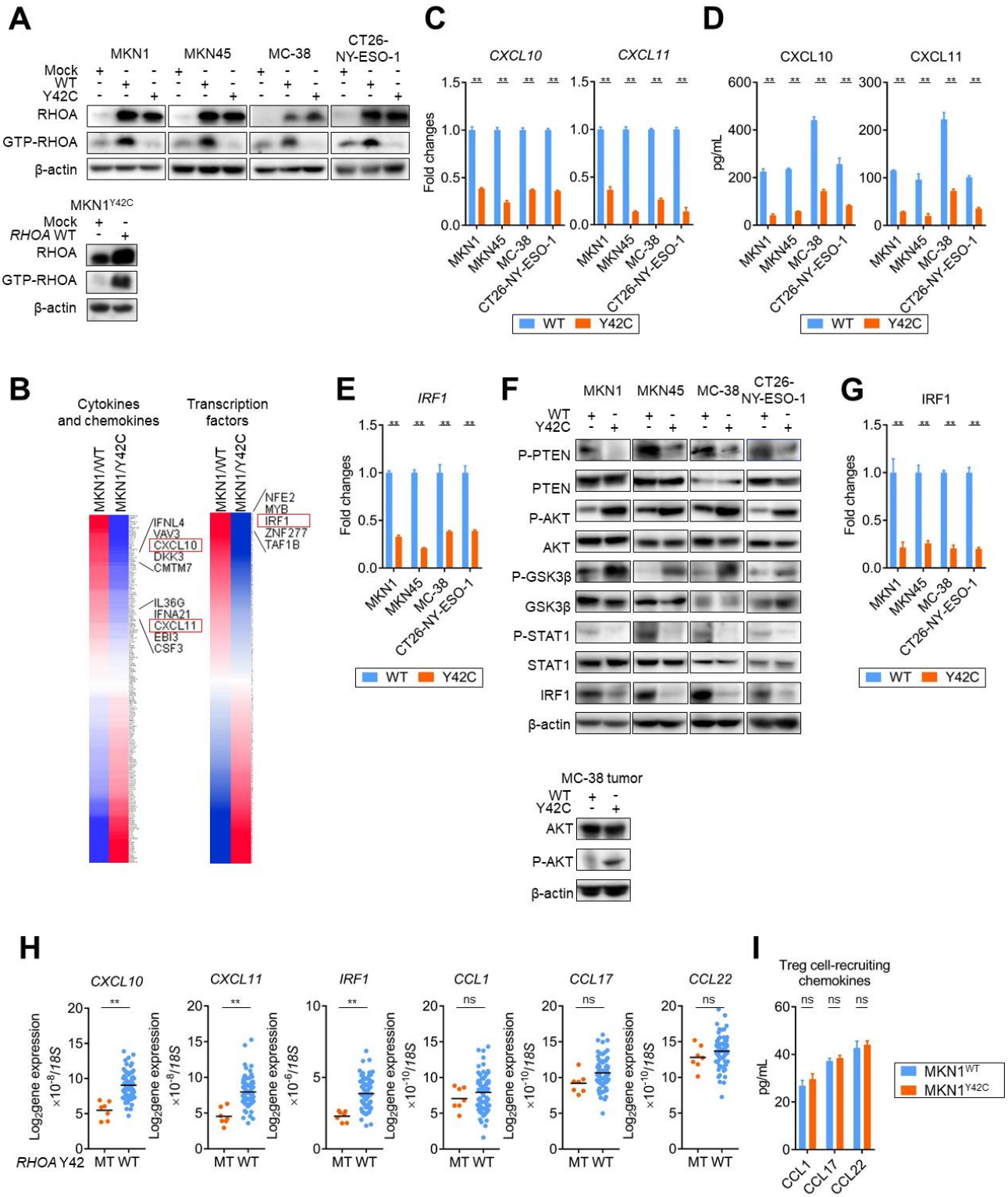

(A) *RHOA* WT or *RHOA* Y42C was retrovirally transduced into two human GC cell lines (MKN1 and

MKN45) and two murine gastrointestinal cell lines (MC-38 and CT26-NY-ESO-1) (upper). *RHOA* Y42C was retrovirally transduced into MKN1^{Y42C} (lower). Representative blots of Rhotekin pulldown assays from three independent experiments are shown. **(B)** MKN1^{WT} and MKN1^{Y42C} cells were subjected to microarray analysis. The expression of cytokines and chemokines (left) or transcriptional factors (right) based on gene ontology (GO) terms was compared. **(C)** *CXCL10* and *CXCL11* expression in *RHOA* WT- or Y42C-overexpressing cell lines was examined with real-time qRT-PCR. Fold changes relative to the *RHOA* WT-overexpressing cell lines are shown. **(D)** The concentrations of CXCL10 and CXCL11 in the culture of *RHOA* WT- or Y42C-overexpressing cell lines were analyzed by ELISA. *RHOA* WT- and Y42C-overexpressing cell lines were cultured with RPMI medium containing 10% FBS. Forty-eight hours later, the concentrations of CXCL10 and CXCL11 were examined. **(E)** *IRF1* expression in *RHOA* WT- or Y42C-overexpressing cell lines was evaluated with real-time qRT-PCR. Fold changes relative to the *RHOA* WT-overexpressing cell lines are shown. **(F and G)** The protein expression of PI3K-AKT signaling pathways in *RHOA* WT- or Y42C-overexpressing cell lines was examined by western blotting **(F, upper)**. MC-38^{WT} or MC-38^{Y42C} cells (1.0×10^6) were injected subcutaneously into C57BL/6 mice on day 0 (N = 3). Protein was extracted from the tumors on day 12. The protein expression of total and phosphorylated AKT in MC-38^{WT} or MC-38^{Y42C} tumors was examined by western blotting. Representative blots of western blotting are shown **(F, lower)**. Summary of quantified IRF1 (IRF1/β-actin) expression in Y42C-overexpressing cell lines relative to that in *RHOA* WT-overexpressing cell lines from three independent experiments is shown (**G**). Means from three independent experiments are presented. (**H**) Gene expression in advanced GC samples according to *RHOA* gene status was examined by real-time qRT-PCR. **(I)** The concentrations of CCL1, CCL17, and CCL22 in the culture medium of MKN1^{WT} or MKN1^{Y42C} were analyzed by ELISA. MKN1^{WT} or MKN1^{Y42C} were cultured with RPMI medium containing 10% FBS. Forty-eight hours later, the concentrations of CCL1, CCL17, and CCL22 were examined. β-actin and *18S* ribosomal RNA were used as internal controls for protein and mRNA expression analyses, respectively. Bars, mean; error bars, SEM; **, $P < 0.01$; and MT, mutation; WT, wild-type.

Figure 3. *RHOA* Y42 mutations promote Treg cell survival through increased FFA production.

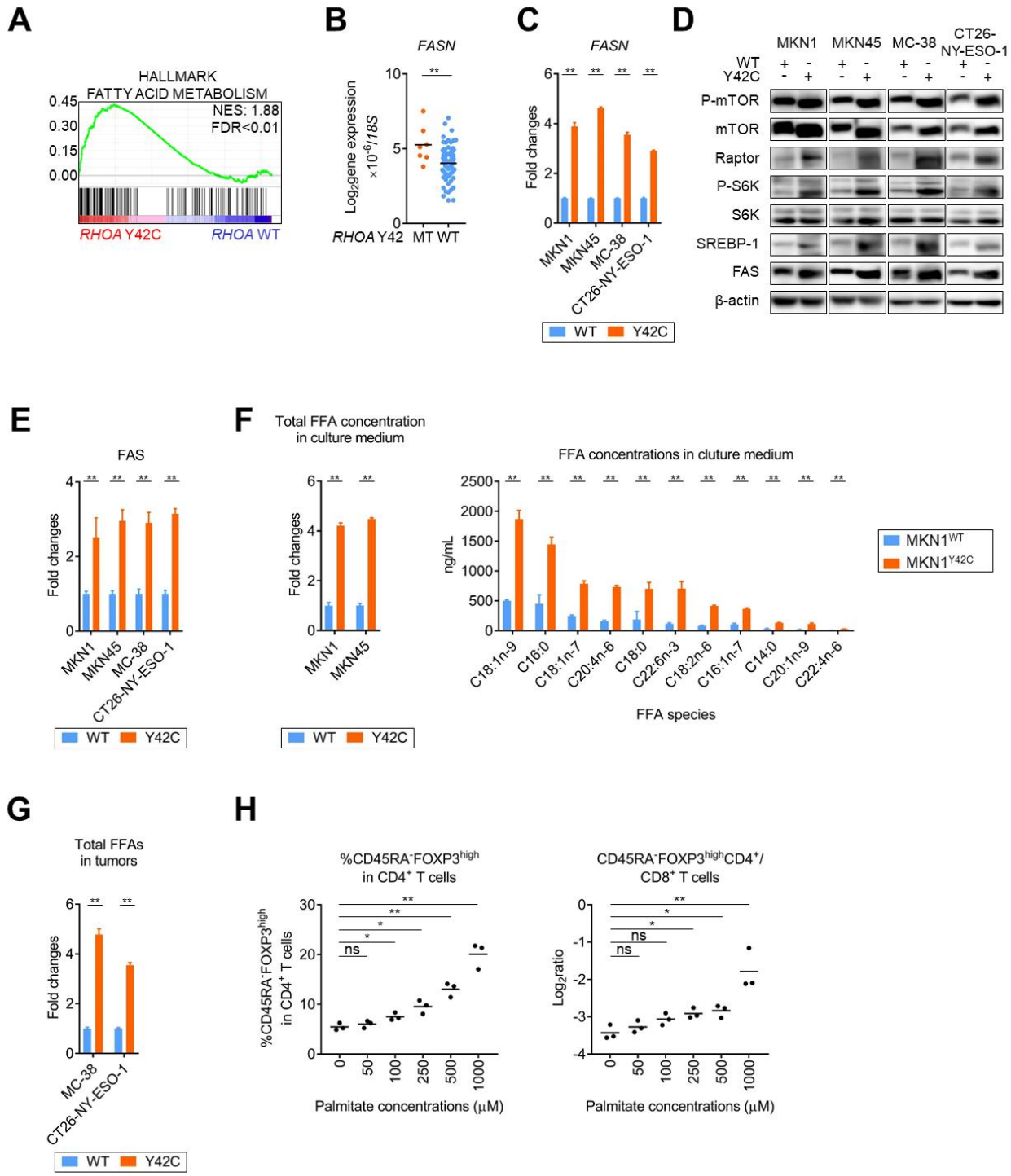

(A) Fatty acid metabolism-related genes based on GSEA in *RHOA* Y42 mutated-GCs were compared with those in *RHOA* WT-GCs using RNA-seq data from surgically-resected GC samples. **(B)** *FASN*

expression in advanced GC samples according to *RHOA* gene status was examined by real-time qRT-PCR. **(C)** *FASN* expression in *RHOA* WT- or Y42C-overexpressing cell lines was analyzed with real-time qRT-PCR. Fold changes relative to the *RHOA* WT-overexpressing cell lines are shown. **(D and E)** The protein expression of mTORC1 signaling pathway components in *RHOA*-overexpressing cell lines was examined by western blotting (**D**). Summary of quantified FAS (FAS/β-actin) expression in Y42C-overexpressing cell lines relative to that in *RHOA* WT-overexpressing cell lines from three independent experiments is also shown (**E**). **(F)** FFA concentrations in the culture were evaluated using the Free Fatty Acid Quantification Kit (left) and LC-MS (right). *RHOA*-overexpressing cell lines were cultured with RPMI medium containing 10% lipids-without FBS. Forty-eight hours later, the concentrations of FFAs were examined. **(G)** MC-38^{WT}, MC-38^{Y42C}, CT26-NY-ESO-1^{WT} or CT26-NY-ESO-1^{Y42C} cells (1.0×10^6) were injected subcutaneously into C57BL/6 mice on day 0 (N = 3 per group). Tumor interstitial fluids were extracted from the *RHOA*-overexpressing MC-38 and CT26-NY-ESO-1 tumors on day 12. Total FFAs in the interstitial fluids of the *RHOA* WT- or *RHOA* Y42C-overexpressing MC-38 and CT26-NY-ESO-1 tumors were evaluated by the Free Fatty Acid Quantification Kit. All *in vivo* experiments were performed at least twice. **(H)** The frequency of eTreg cells in low-glucose culture medium with the indicated palmitate concentration was assessed. PBMCs stimulated with anti-CD3 mAb and anti-CD28 mAb were cultured in glucose-free RPMI medium supplemented with 10% lipids without FBS, low-glucose (1 mM) and the indicated concentration of palmitate-BSA. Seventy-two hours later, the PBMCs were subjected to FCM. Means from three independent experiments are shown. β-actin and *18S* ribosomal RNA were used as internal controls for protein and mRNA expression analyses, respectively. Bars, mean; error bars, SEM; *, $P < 0.05$; **, $P < 0.01$; MT, mutation; WT, wild-type; and ns, not significant.

Figure 4. Treg cells in the TME take up and utilize more FFAs than other T cell subsets, and FFA-producing tumors enhance highly suppressive Treg cells and dampen anti-tumor efficacy of anti-PD-1 mAb.

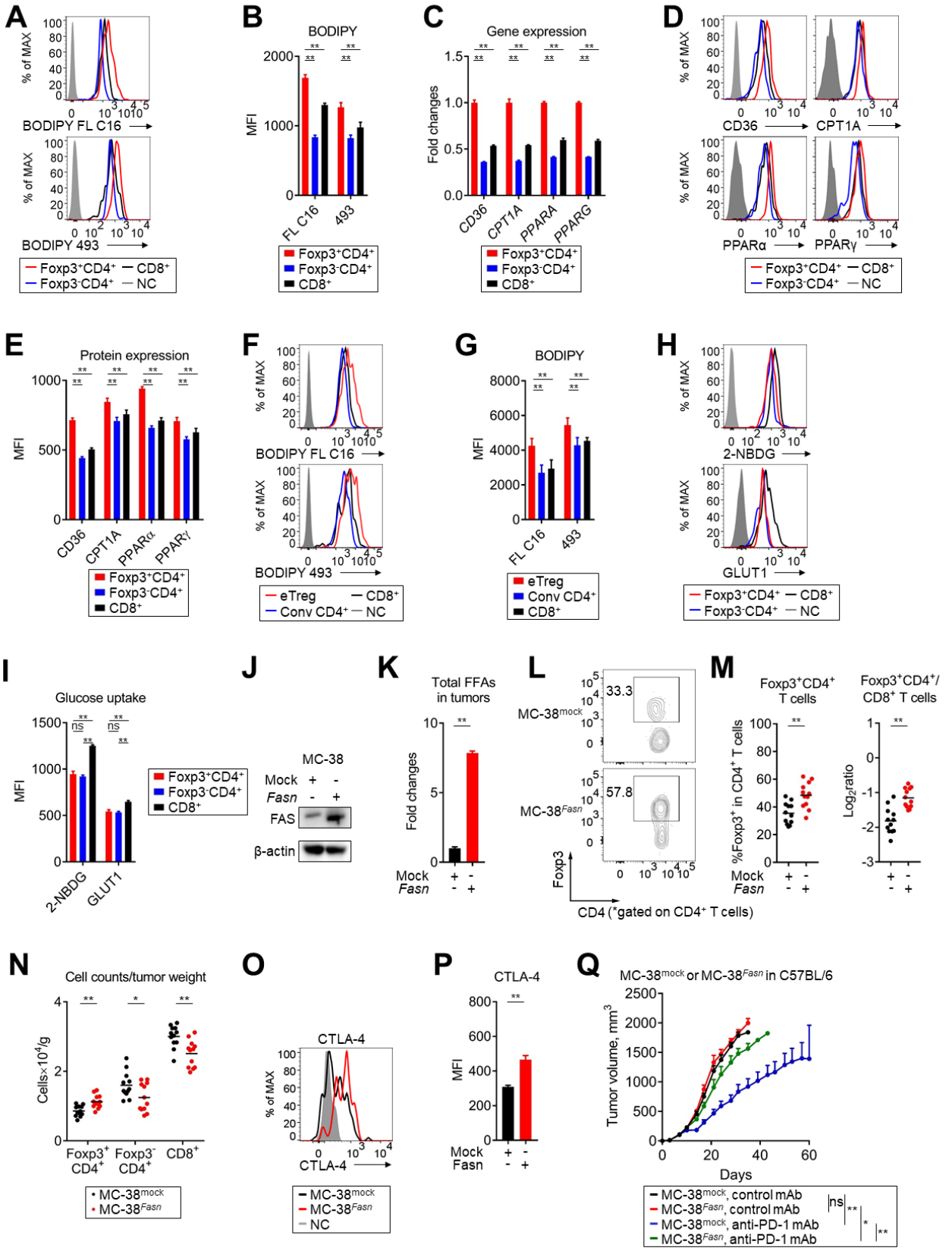

MC-38 cells (1.0×10^6) were injected subcutaneously into *Foxp3*$^{Thy1.1}$ C57BL/6 mice on day 0 (N = 6). TILs on day 12 were subjected to FCM. **(A and B)** The uptake and content of FFAs in TILs were assessed with BODIPY FL C16 and BODIPY 493, respectively. Representative histogram plots (**A**) and MFI summary (**B**) are shown. (**C**) The expression of fatty acid metabolism-related genes (*CD36*, *CPT1A*, *PPARA,* and *PPARG*) in TILs was examined by real-time qRT-PCR. **(D and E)** The expression of FFA metabolism-related molecules (CD36, CPT1A, PPARα, and PPARγ) in TILs was analyzed with FCM. Representative histogram plots (**D**) and MFI summary (**E**) are shown (N = 6). **(F and G)** The uptake and content of FFAs in TILs from human GC clinical samples were analyzed with BODIPY FL C16 and BODIPY 493, respectively (N = 5). Representative histogram plots (**F**) and MFI summary (**G**) are shown. **(H and I)** MC-38 cells (1.0×10^6) were injected subcutaneously into *Foxp3*$^{Thy1.1}$ C57BL/6 mice on day 0 (N = 6). TILs on day 12 were subjected to FCM. Glucose uptake (2-NBDG) and GLUT1 expression in TILs were assessed. Representative histogram plots (**H**) and MFI summaries (**I**) are shown. (**J**) Mock or *Fasn* was retrovirally transduced into MC-38 cells. Representative blots of FAS from three independent experiments are shown. (**K-P**) MC-38^{mock} or MC-38^{Fasn} cells (1.0×10^6) were injected subcutaneously into C57BL/6 mice on day 0. Tumor interstitial fluids or TILs were extracted from the MC-38^{mock} or MC-38^{Fasn} tumors on day 12. **(K)** Total FFAs in the interstitial fluids of the MC-38^{mock} or MC-38^{Fasn} tumors were evaluated by the Free Fatty Acid Quantification Kit (N = 4 per group). **(L-P)** TILs on day12 were subjected to FCM. (**L-N**) The frequencies of Foxp3$^+$CD4$^+$ T cells, the ratio of Foxp3$^+$CD4$^+$ to CD8$^+$ T cells in the TME, and the number of each T cell subset (counts per tumor weight) were examined with FCM (N = 12 per group). Representative contour plots (**L**) and summary (**M and N**) are shown. (**O and P**) CTLA-4 expression by Foxp3$^+$CD4$^+$ T cells in the TME was examined with FCM (N = 6 per group). Representative histograms (**O**) and MFI summary (**P**) are shown. (**Q**) MC-38^{mock} or MC-38^{Fasn} cells (1.0×10^6) were injected subcutaneously into C57BL/6 mice on day 0, and anti-PD-1 mAb or control mAb was administered on days 6, 11, and 16 (N = 12 per group). The tumor growth curves of the indicated groups are shown. NC, negative control; bars, mean; error bars, SEM; and **, $P < 0.01$.

Figure 5. *RHOA* Y42C promotes the development of an immunosuppressive TME.

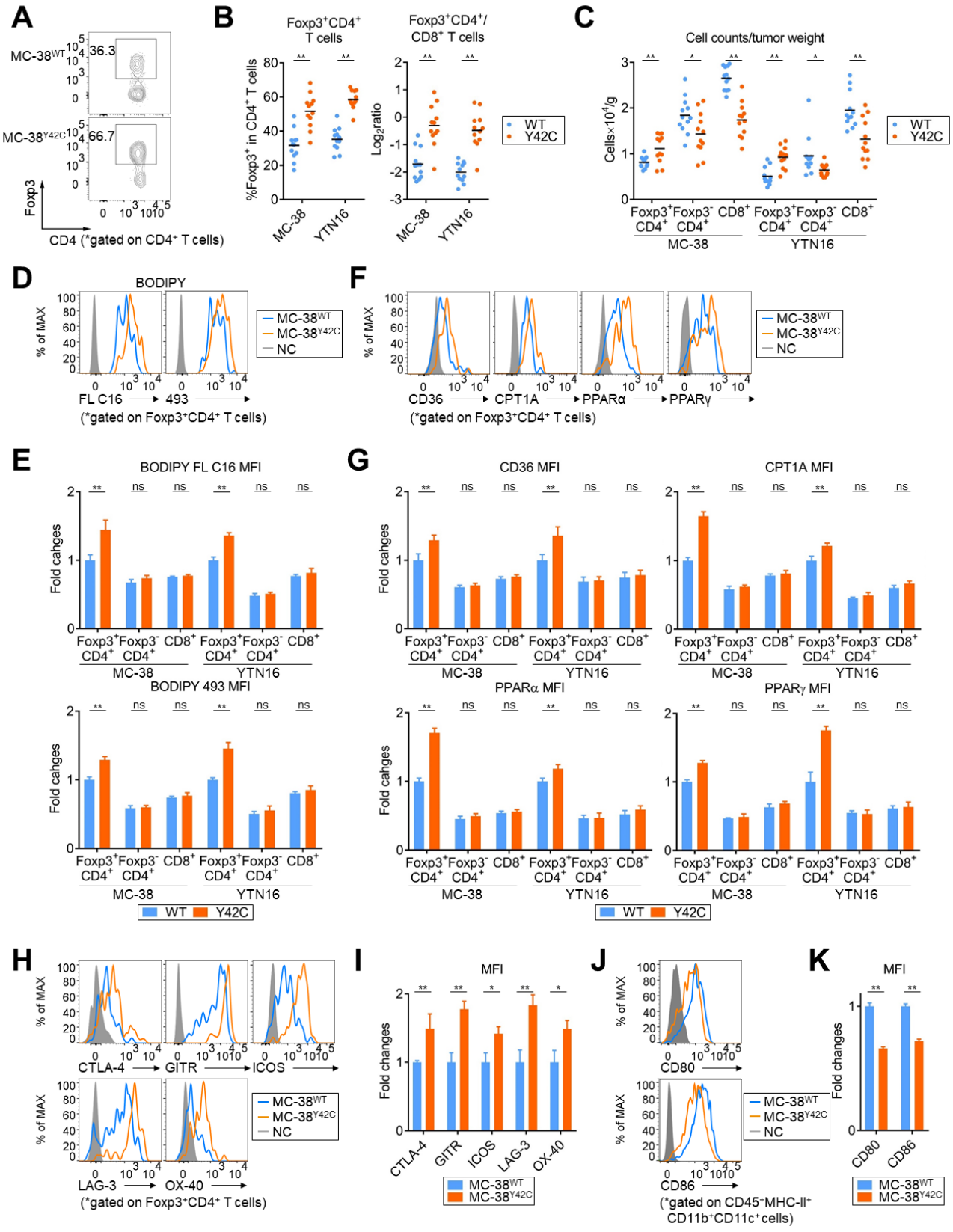

RHOA WT or *RHOA* Y42C was retrovirally transduced into a murine gastric cancer cell line (YTN16^{WT} and YTN16^{Y42C}, respectively). **(A-C)** MC-38^{WT}, MC-38^{Y42C} cells, YTN16^{WT} or

YTN16^{Y42C} (1.0×10^6) were injected subcutaneously into C57BL/6 mice on day 0. TILs on day 12 were subjected to FCM. The frequencies of Foxp3$^+$CD4$^+$ T cells, the ratio of Foxp3$^+$CD4$^+$ to CD8$^+$ T cells in the TME, and the number of each T cell subset (counts per tumor weight) were examined with FCM (N = 12 per group). Representative contour plots (**A**) and summaries (**B and C**) are shown. (**D and E**) MC-38^{WT}, MC-38^{Y42C}, YTN16^{WT} or YTN16^{Y42C} cells (1.0×10^6) were injected subcutaneously into *Foxp3*$^{Thy1.1}$ C57BL/6 mice on day 0 (MC-38^{WT} and MC-38^{Y42C}; N = 3, YTN16^{WT} and YTN16^{Y42C}; N = 5). TILs on day 12 were subjected to FCM. The uptake and content of FFAs in TILs were assessed with BODIPY FL C16 and BODIPY 493, respectively. Representative histogram plots (**D**) and MFI summaries (**E**) are shown. **(F-K)** MC-38^{WT}, MC-38^{Y42C} **(F-K)**, YTN16^{WT} or YTN16^{Y42C} cells **(F and G)** (1.0×10^6) were injected subcutaneously into C57BL/6 mice on day 0 (MC-38^{WT} and MC-38^{Y42C}; N = 3, YTN16^{WT} and YTN16^{Y42C}; N = 5). TILs prepared from tumor tissue samples on day 12 were subjected to FCM. The expression of fatty acid metabolism-related molecules (CD36, CPT1A, PPARα, and PPARγ) in TILs was analyzed with FCM. Representative histogram plots (**F**) and MFI summaries (**G**) are shown. (**H and I**) The expression of CTLA-4, GITR, ICOS, LAG-3, and OX-40 by Foxp3$^+$CD4$^+$ T cells in the TME was examined with FCM (N = 6 per group). Representative histograms (**H**) and MFI summaries (**I**) are shown. **(J and K)** The expression of CD80 and CD86 by tumor-infiltrating APCs (detected as CD45$^+$MHC-II$^+$CD11b$^+$CD11c$^+$ cells) was analyzed (N = 6 per group). Representative histogram plots (**J**) and MFI summaries (**K**) are shown. NC, negative control; bars, mean; error bars, SEM; *, $P<0.05$; **, $P < 0.01$; and ns, not significant.

Figure 6. Abundant FFAs in *RHOA* Y42C tumors induce the resistance to anti-PD-1 mAb treatment.

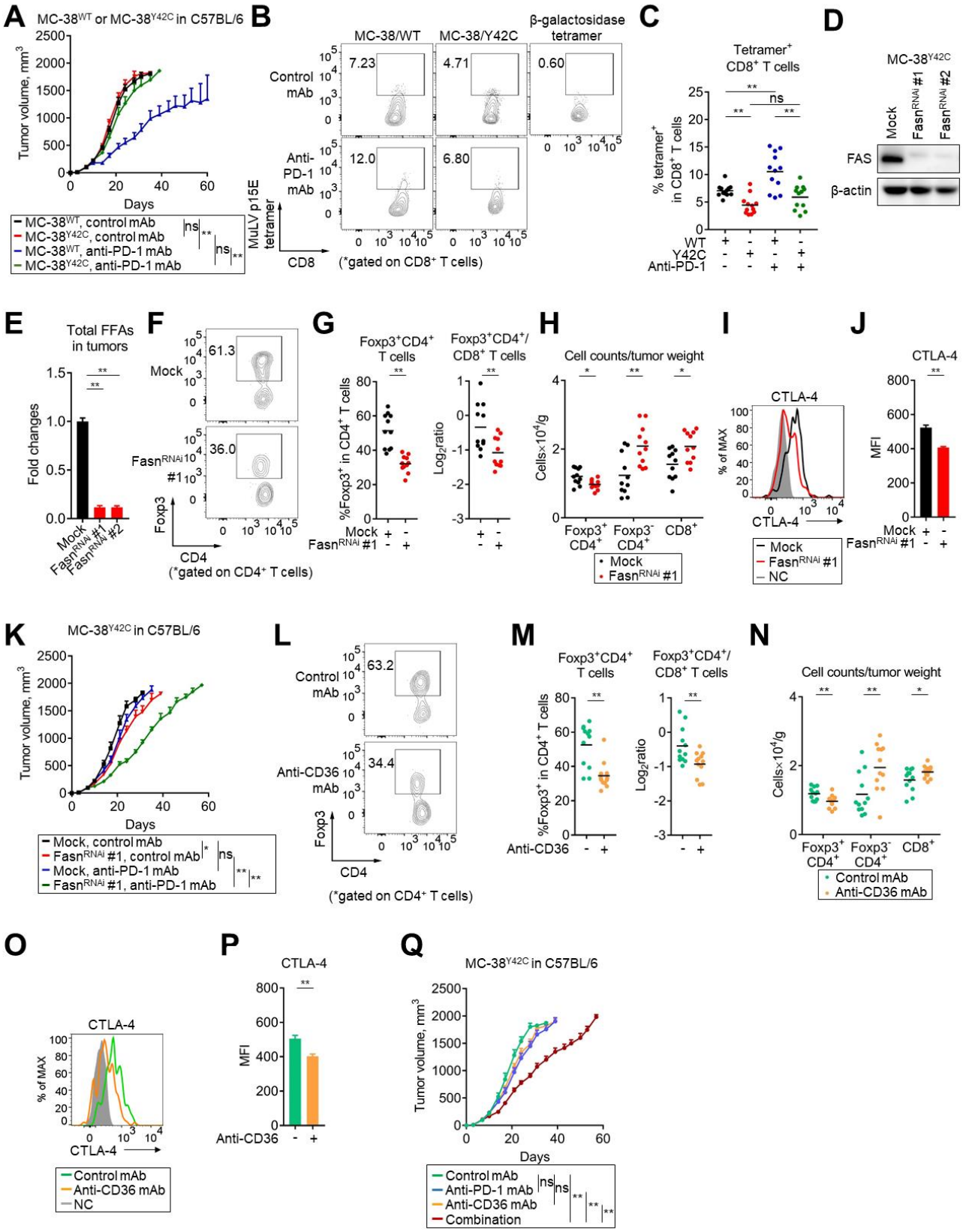

(A-C) MC-38^{WT} or MC-38^{Y42C} cells (1.0×10^6) were injected subcutaneously into C57BL/6 mice on

day 0, and anti-PD-1 mAb or control mAb was administered on days 6, 11, and 16 (N = 12 per group). The tumor growth curves of the indicated groups are shown in (**A**). TILs on day 12 were subjected to FCM. MC-38 antigen-specific $CD8^+$ T cells were detected by MuLV p15E/H-2Kb tetramers (N = 12 per group). Representative contour plots (**B**) and summary (**C**) are shown. β-galactosidase/H-2Kb tetramer staining served as a control. (**D-K**) shNC or sh*Fasn* was lentivirally transduced into MC-38^{Y42C} cells. Representative blots of FAS from three independent experiments are shown **(D)**. (**E-J**) MC-38^{Y42C}-shNC or MC-38^{Y42C}-sh*Fasn* cells (1.0×10^6) were injected subcutaneously into C57BL/6 mice on day 0. Tumor interstitial fluids or TILs were extracted from the MC-38^{Y42C}-shNC or MC-38^{Y42C}-sh*Fasn* tumors on day 12. **(E)** Total FFAs in the interstitial fluids of the MC-38^{Y42C}-shNC or MC-38^{Y42C}-sh*Fasn* tumors were evaluated by the Free Fatty Acid Quantification Kit (N = 4 per group). **(F-J)** TILs on day 12 were subjected to FCM. (**F-J**) The frequencies of $Foxp3^+CD4^+$ T cells, the ratio of $Foxp3^+CD4^+$ to $CD8^+$ T cells in the TME, and the number of each T cell subsets (cell counts per tumor weight) were examined with FCM (N = 11 per group). The expression of CTLA-4 by $Foxp3^+CD4^+$ T cells in the TME was examined with FCM (N = 6 per group). Representative contour plots (**F**) or histograms **(I)** and summaries (**G, H, and J**) are shown. (**K**) MC-38^{Y42C}-shNC or MC-38^{Y42C}-sh*Fasn* cells (1.0×10^6) were injected subcutaneously into C57BL/6 mice on day 0, and anti-PD-1 mAb or control mAb was administered on days 6, 11, and 16 (N = 12 per group). The tumor growth curves of the indicated groups are shown. (**L-P**) MC-38^{Y42C} cells (1.0×10^6) were injected subcutaneously into C57BL/6 mice on day 0. Anti-CD36 mAb or control mAb was administered daily (N = 12 per group). TILs prepared from tumor tissue samples on day 12 were subjected to FCM. (**L-N**) The frequencies of $Foxp3^+CD4^+$ T cells, the ratio of $Foxp3^+CD4^+$ to $CD8^+$ T cells in the TME, and the number of each T cell subsets (cell counts per tumor weight) were examined with FCM (N = 12 per group). The expression of CTLA-4 by $Foxp3^+CD4^+$ T cells in the TME was examined with FCM (N = 6 per group). Representative contour plots or histograms (**L and O**) and summaries (**M, N, and P**) are shown. (**Q**) MC-38^{Y42C} cells (1.0×10^6) were injected subcutaneously into C57BL/6 mice on day 0, and anti-PD-1 mAb (intravenously, on days 6, 11, and 16) and/or anti-CD36 mAb (intravenously, daily) was administered (N = 12 per group). The tumor growth curves of the indicated groups are shown. NC, negative control; bars, mean; error bars, SEM; *, $P<0.05$; **, $P < 0.01$; and ns, not significant.

Figure 7. The combination with a PI3Kβ inhibitor or anti-CTLA-4 mAb overcomes the resistance of *RHOA* Y42C tumors to anti-PD-1 mAb.

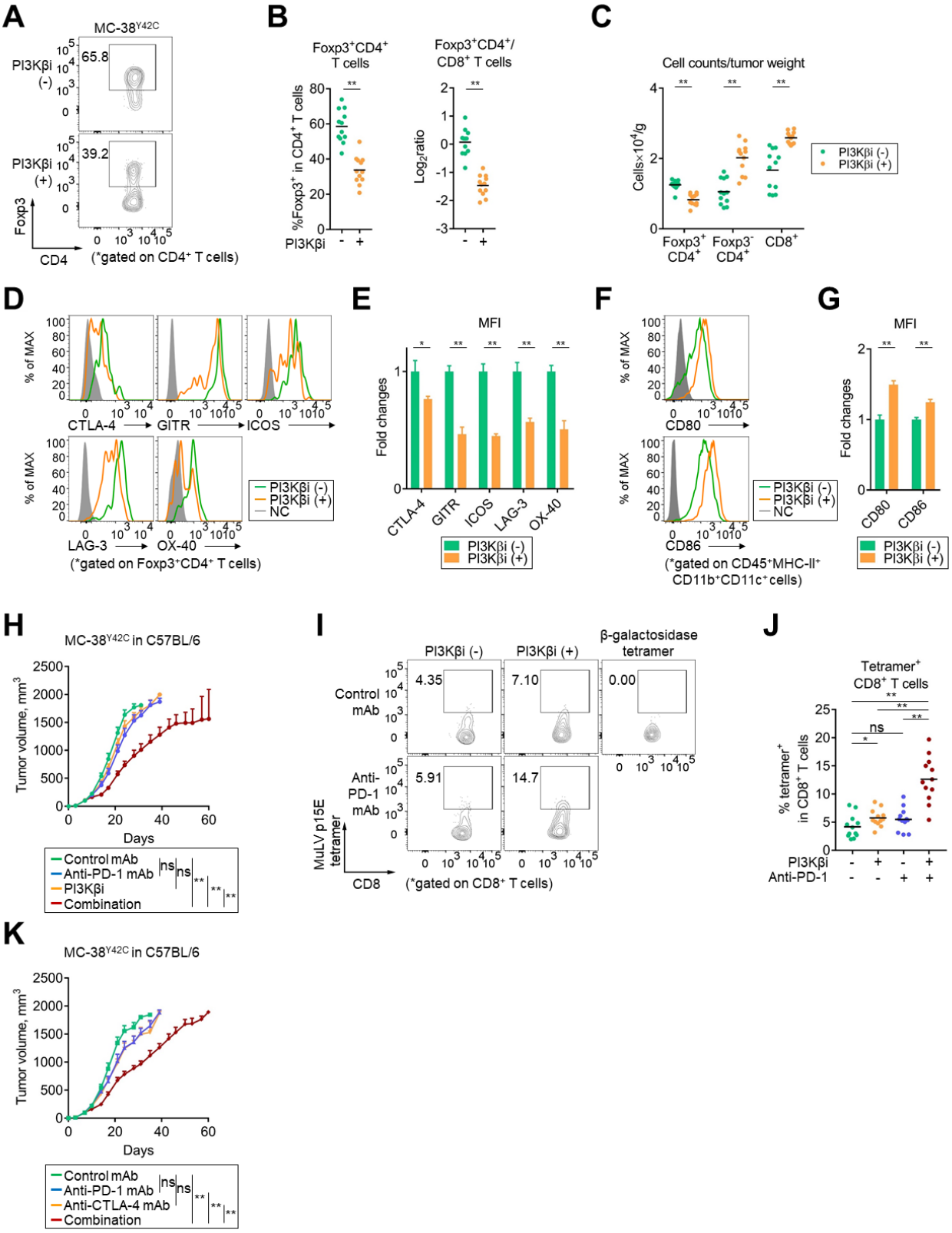

(A-G) MC-38^{Y42C} cells (1.0×10^6) were injected subcutaneously into C57BL/6 mice on day 0, and

GSK2636771 was orally administered for five days. TILs on day 12 were subjected to FCM. Representative contour plots for CD4 and Foxp3 **(A)** and summaries **(B and C)** are shown (N = 12 per group). **(D and E)** The expression of CTLA-4, GITR, ICOS, LAG-3, and OX-40 by $Foxp3^{+}CD4^{+}$ T cells in the TME was evaluated (N = 6 per group). Representative histogram plots **(D)** and MFI summaries are shown **(E)**. **(F and G)** The expression of CD80 and CD86 by APCs in the TME was examined (N = 6 per group). Representative histogram plots **(F)** and MFI summaries **(G)** are shown. **(H-J)** MC-38^{Y42C} cells (1.0×10^{6}) were injected subcutaneously into C57BL/6 mice on day 0. The mice were treated with anti-PD-1 mAb (intravenously, on days 6, 11, and 16) and/or GSK2636771 (orally, for five days) (N = 12 per group). The tumor growth curves of the indicated groups are shown in **(H).** TILs were prepared from tumor tissue samples on day 12, and tumor antigen-specific $CD8^{+}$ T cells were detected by MuLV p15E/H-2Kb tetramers (N = 12 per group). Representative contour plots **(I)** and summary **(J)** are shown. β-galactosidase/H-2Kb tetramer staining served as a control. (**K**) MC-38^{Y42C} cells (1.0×10^{6}) were injected subcutaneously into C57BL/6 mice on day 0. These mice were treated with anti-PD-1 mAb (intravenously, on days 6, 11, and 16) and/or anti-CTLA-4 mAb (intravenously, on days 6, 11, and 16) (N = 12 per group). The tumor growth curves of the indicated groups are shown. NC, negative control; bars, mean; error bars, SEM; PI3Kβi, PI3Kβ inhibitor; *, $P<0.05$; **, $P < 0.01$; and ns, not significant.

STAR Methods

CONTACT FOR REAGENT AND RESOURCE SHARING

Further information and requests for resources and reagents should be directed to and will be fulfilled by the Lead Contact, Hiroyoshi Nishikawa (hnisihika@ncc.go.jp).

EXPERIMENTAL MODEL AND SUBJECT DETAILS

Patients and samples

Twenty-three patients with GC who underwent surgical resection at National Cancer Center Hospital East between 2015 and 2016 and ninety-five patients (eighty-five patients for immunological analysis, seven patients for BODIPY analysis and three patients with *RHOA* mutations who received anti-PD-1 mAb) with advanced GC who underwent endoscopic biopsy were enrolled in this study (summarized in Tables S1-S4). PBMCs were isolated by density gradient centrifugation with Ficoll-Paque (GE Healthcare, Chicago, IL). To collect TILs, tumor tissue samples were minced and treated with gentleMACS Dissociator (Miltenyi Biotec, Bergisch Gladbach, Germany) as described previously (Saito et al., 2016; Tada et al., 2018). All patients provided written informed consent before sampling, according to the Declaration of Helsinki. This study was performed in a blinded manner and was approved by the National Cancer Center Ethics Committee.

Cell lines and reagents

MKN1 and MKN45 human GC cell lines were obtained from the Japanese Collection of Research Bioresources (JCRB; Osaka, Japan; JCRB Cat#JCRB0252, RRID: CVCL_1415) and American Type Culture Collection (ATCC; Manassas, VA; ATCC Cat#CRL-1739, RRID: CVCL_0434), respectively. MC-38 and CT26 mouse colon cancer cell lines were obtained from Kerafast (Boston, MA; Cat#ENH204, RRID: B288) and ATCC (Cat#CRL-2638, RRID: CVCL_7254), respectively. YTN16 mouse gastric adenocarcinoma cell line was developed as describe previously (Yamamoto et al., 2018). CT26-NY-ESO-1 cell line is a cell line derived from CT26 cells stably transfected with NY-ESO-1 (Muraoka et al., 2010). All cell lines were maintained in RPMI medium (Fujifilm Wako Pure Chemical Corporation, Osaka, Japan) supplemented with 10% fetal bovine serum (FBS; Biosera, Orange, CA). The human *RHOA* (wild-type or Y42C mutation)-overexpressing cell lines were established via retroviral transduction using a pBabe-puro vector (Addgene, Cat#1764, Cambridge, MA) or a pMMLV-neo vector (VectorBuilder, Chicago, IL). The murine Fasn-overexpression cell line was established with retroviral transduction using a pMMLV-neo vector (VectorBuilder). The murine Fasn knocked-down cell lines were established by lentiviral transduction using SMARTvector lentiviral shRNA (Horizon Discovery, Cambridge, UK) and growth from a single clone. GSK2636771 was obtained from Selleck (Houston, TX). Anti-PD-1 mAb (4H2) was kindly provided by Ono Pharmaceutical (Osaka, Japan), and anti-CTLA-4 mAb (9H10) was obtained from BioLegend (San Diego, CA). The control rat IgG mAb (RTK2758) used in the *in vivo* study was obtained from BioLegend. The anti-CD36 mAb (JC63.1) and the control mouse IgA (S107) were obtained from

Abcam (Cambridge, UK).

In vivo animal models

Female C57BL/6, BALB/c, and BALB/c-*nu/nu* mice (6- to 10-week-old females; CLEA Japan, Tokyo, Japan) and *Foxp3*$^{Thy1.1}$ C57BL/6 mice (6 to 10 weeks old; The Jackson Laboratory, Bar Harbor, MA: kindly provided by Dr. Alexander Rudensky in Memorial Sloan Kettering Cancer Center, NY, NY) were used for the *in vivo* studies. Animal care and experiments were conducted according to the guidelines of the animal committee of the National Cancer Center after approval by the Ethics Review Committee for Animal Experimentation of the National Cancer Center. A suspension of 1×10^6 cells (in 100 μL of PBS) was subcutaneously inoculated. In some groups, anti-PD-1 mAb (200 μg/body) was administered intravenously three times at five-day intervals with or without GSK2636771 (30 mg/kg) administered orally for five days. In other experiments, anti-CD36 mAb (10 μg/body) was administered intravenously daily combined with or without anti-PD-1 mAb, and anti-CTLA-4 mAb (100 μg/body) was administered intravenously three times at five-day intervals combined with or without anti-PD-1 mAb. Tumor volume was calculated as the length × width^2 × 0.5. Mice were monitored twice a week and sacrificed when tumor volume was >1800 mm^3. For TIL analyses, tumors were collected twelve days after tumor cell injection. Cell counts were calculated with FCM and cell counts per weight were evaluated. To examine antigen-specific CD8$^+$ T cells, T-Select H-2Kb MuLV p15E Tetramer-KSPWFTTL-APC (MBL, Nagoya, Japan) was used according to the manufacturer's

instructions. For intracellular cytokine assays, cells were stimulated for 5 hours with phorbol 12-myristate 13-acetate (PMA; 100 ng/mL)/ionomycin (2 μg/mL) (Sigma-Aldrich, St. Louis, MO). GolgiPlug reagent (1.3 μl/mL) (BD Biosciences, Franklin Lakes, NJ) was added for the last 4 hours of culturing, and then stained cells were subjected to FCM. All *in vivo* experiments were performed at least twice.

RNA-seq

Total RNA was extracted with an RNeasy Mini Kit (Qiagen, Hilden, Germany) according to the manufacturer's instructions. RNA integrity was evaluated with TapeStation (Agilent Technologies, Santa Clara, CA). Complementary DNA (cDNA) was prepared from the isolated RNA using the NEBNext Ultra Directional RNA Library Prep Kit (New England BioLabs, Ipswich, MA), in which cDNA was prepared from polyA-selected RNA. The prepared RNA-seq libraries underwent next-generation sequencing of 120 bp from both ends (paired-end reads) with a HiSeq2500 platform (Illumina, San Diego, CA). For expression profiling with the RNA-seq data, paired-end reads were aligned to the hg38 human genome assembly using TopHat2 (https://ccb.jhu.edu/software/tophat/index.shtml) (Kim et al., 2013). The expression level of each RefSeq gene was calculated from the mapped read counts using Cufflinks (http://cufflinks.cbcb.umd.edu) (Trapnell et al., 2012).

WES and mutational analysis

DNA was extracted with the QIAmp DNA Mini Kit (QIAGEN) according to the manufacturer's instructions. Sequencing libraries were prepared for WES with the NEBNext Ultra DNA Library Prep Kit (New England BioLabs) according to the manufacturer's instructions. Adaptor-ligated samples were amplified with six PCR cycles. The amplified DNA fragments underwent enrichment of the exonic fragments using the SureSelect Human All Exon Kit v5 (Agilent Technologies). Massively parallel sequencing of the isolated fragments was performed with a HiSeq2500 platform (Illumina). Paired-end WES reads were independently aligned to the human reference genome (hg38) using BWA (Li and Durbin, 2009), Bowtie2 (http://bowtie-bio.sourceforge.net/bowtie2/index.shtml), and NovoAlign (http://www.novocraft.com/products/novoalign/). Somatic mutations were called using MuTect (http://www.broadinstitute.org/cancer/cga/mutect), SomaticIndelDetector (http://www.broadinstitute.org/cancer/cga/node/87), and VarScan (http://varscan.sourceforge.net). Mutations were discarded if (I) the read depth was < 20 or the variant allele frequency (VAF) was < 0.1, (II) they were supported by only one strand of the genome, or (III) they were present in the normal human genomes in either the 1000 Genomes Project dataset (http://www.internationalgenome.org/) or our in-house database. Gene mutations were annotated by SnpEff (http://snpeff.sourceforge.net).

Digital PCR and detection of mutations

DNA from eighty-five advanced GC samples were analyzed with digital PCR, using Taqman (Thermo

Fisher Scientific, Waltham, MA) Rare Mutation Assays for *RHOA* Y42C or Y42S on QuantStudio® 3D Digital PCR System (Thermo Fisher Scientific). Data was assessed with QuantStudio® 3D Analysis Suite™ Cloud Software. The automatic call assignments for each data cluster where manually adjusted when needed. The analysis of digital PCR data was performed blinded to the clinical information by two independent investigators (S.K. and Y.T.). The result of the assay was reported as mutant allele frequency (MAF) which was defined as the ratio of mutant DNA molecules per the sum of wild-type DNA molecules and mutant DNA molecules. Samples were considered as positive when MAF was greater than 1.0%.

Gene expression data analysis

Hierarchical cluster analysis of our RNA-seq dataset was performed according to previously reported gene sets using the statistical software R version 3.1.1 (R Foundation for statistical computing, Vienna, Austria); $CD4^+$ Treg cells, $CD8^+$ T cell, co-stimulation APC and T cell, co-inhibition APC and T cell, and cytolytic activity (Rooney et al., 2015). Enriched pathways were determined using the GSEA tool available from the Broad Institute website. Hallmark gene sets were downloaded from the MSigDB database (Subramanian et al., 2005).

FCM analysis

FCM staining and analysis were performed as described (Tada et al., 2018; Takeuchi et al., 2018). The

antibodies used in the FCM analyses are summarized in Key Resource Table. Cells were washed with a washing solution and subjected to staining with surface antibodies and a fixable viability dye (Thermo Fisher Scientific). Then, intracellular staining was performed with intracellular antibodies and the Foxp3/Transcription Factor Staining Buffer Set (Thermo Fisher Scientific) according to the manufacturer's instructions. After washing, the cells were analyzed with an LSR Fortessa or Symphony instrument (BD Biosciences) and FlowJo software (BD Biosciences).

BODIPY or 2-NBDG analysis

For assessment of fatty acid uptake, fatty acid content, and glucose uptake, cells isolated from blood and tumor tissue were immediately incubated with 0.5 μM BODIPY FL C16, 0.5 μM BODIPY 493, or 100 μM 2-NBDG, respectively, (Thermo Fisher Scientific) for 30 min at 37°C. The cells were washed twice with cold PBS and subsequently subjected to FCM.

Apoptosis analysis

Apoptosis was assessed by FCM with FITC-annexin V, 7-AAD (Thermo Fisher Scientific), and active caspase-3 staining. The dilution of the staining reagents was performed according to the manufacturer's instructions.

Proliferation analysis

Proliferation was evaluated by dilution of Carboxyfluorescein succinimidyl ester (CFSE, Thermo Fisher Scientific)-labelled cells with FCM. The dilution of the staining reagents was performed according to the manufacturer's instructions.

IHC

Multiplexed fluorescent IHC was performed with the Tyramide Signal Amplification method using the Opal IHC kit (PerkinElmer, Waltham, MA) according to the instructions provided by the manufacturer. Anti-human CD8 (clone C8/144b, DAKO, Glostrup, Denmark), anti-human CD4 (clone 4B12, DAKO), anti-human CD3 (clone SP7, Abcam), and anti-human FOXP3 (clone 236A/E7, Abcam) mAbs were used for primary staining. A horseradish peroxidase-labelled secondary detection system (EnVision plus, DAKO) was employed as a catalyst for fluorophore-conjugated tyramide. Multiplexed fluorescence-labelled images of randomly selected fields (669 x 500 μm each) were captured with an automated imaging system (Vectra ver. 3.0, PerkinElmer). Image analysis software (InForm, PerkinElmer) was used to segment cells and define specific phenotypes. Cells positive for CD8, CD4, and FOXP3 were counted in five high-powered microscopic fields (400x; 0.0625 mm^2), and their averages were calculated. Two researchers (S.K. and E.S.) independently evaluated the stained slides.

Real-time qRT-PCR and microarray

RNA was extracted using the RNeasy Mini Kit (QIAGEN), cDNA was generated using SuperScript

VILO (Thermo Fisher Scientific), and real-time qRT-PCR was performed with Taqman Gene Expression reagents (Thermo Fisher Scientific) (for clinical samples) or SYBR Green reagents (Thermo Fisher Scientific) (for non-clinical samples) using the QuantStudio 7 Flex Real-Time PCR System (Thermo Fisher Scientific). Gene expression changes relative to the expression of *18S* ribosomal RNA, which was used as a housekeeping gene, were calculated using the DDCT method. Microarray analyses were performed with the Clariom S array according to the manufacturer's instructions (Thermo Fisher Scientific). The primers used in this study are listed in Key Resources Table.

ELISA

The concentrations of human CXCL10, CXCL11, CCL1, CCL17, and CCL22 and of murine CXCL10 and CXCL11 were examined with specific sandwich ELISAs according to the manufacturer's instructions (R&D Systems, Minneapolis, MI).

Western blotting

Sub-confluent cells or tumors were washed with PBS and harvested with M-PER (Thermo Fisher Scientific). Whole-cell lysates were separated by SDS-PAGE and blotted onto a polyvinylidene fluoride membrane. After blocking, the membrane was probed with the primary antibody. After rinsing twice with a TBS buffer, the membrane was incubated with a horseradish peroxidase-conjugated

secondary antibody and washed, followed by visualization using an ECL detection system and a LAS-4000 (GE Healthcare, Chicago, IL). The antibodies used for western blotting are summarized in Key Resource Table. Each band intensity is given relative to the corresponding band intensity of β-actin and was quantified by ImageJ (ver1.51).

Rhotekin binding assays

The amount of the GTP-bound form of the RHOA protein was evaluated with a RhoA Activation Assay kit (Cytoskeleton) (Denver, CO) according to the manufacturer's instructions. Briefly, a cell lysate was incubated at 4°C for one hour with a GST fusion protein containing the RHO-binding domain of rhotekin (GST-RBD) immobilized on glutathione-Sepharose beads. After washing, the bead-bound proteins were fractionated with SDS-PAGE and immunoblotted with an anti-RHOA antibody. The total cell lysate was also blotted with the anti-RHOA antibody to assess the fractional ratio of rhotekin-bound RHOA protein.

Assay measuring the FFA concentration or the Glucose concentration

To quantify the FFA concentration in culture medium, all the cell lines were maintained in RPMI medium supplemented with 10% lipids without FBS (Biowest, Nuaillé, France). Plasma was subtracted from blood and interstitial fluids from tumors were collected by centrifugation as previously described (Wiig et al., 2003). The concentrations of total FFAs or glucose were assessed with the Free

Fatty Acid Quantification Kit (BioVision, Zurich, Switzerland) or the Glucose Assay Kit (BioVision). The concentrations of FFA species were determined by LC-MS.

LC-MS assay for FFA species

LC-MS assay was employed to determine the FFA species concentrations in culture medium. LC was performed with an LC-20ADXR ternary pump system equipped with a DGU-20A5R degassing unit, an SIL-20AC autosampler, and a CTO-20AC column oven (Shimadzu Co., Ltd., Kyoto, Japan). The LC system was coupled with an LTQ Orbitrap XL hybrid linear ion trap-Fourier transform mass spectrometer (Thermo Fisher Scientific). FFAs were detected by obtaining the extracted ion chromatograms of the deprotonated ions ([M-H]-) at a mass tolerance of 10 ppm. Instrument control, data acquisition, and data processing were achieved using Xcalibur 2.1.0 software (Thermo Fisher Scientific).

PBMC culture with palmitate

Palmitate (Nacalai Tesque, Kyoto, Japan) or oleate (Fujifilm Wako) was dissolved in 100% ethanol at 200 mM and conjugated to fatty acid-free BSA at a 5:1 molar ratio at a final concentration of 8 mM palmitate- or oleate-BSA by vortexing at 37°C for 3-4 hours with sonication. $CD45RA^{-}CD25^{high}CD4^{+}$ T cells (eTreg cells), $CD45RA^{-}CD25^{-}CD4^{+}$ T cells (conv $CD4^{+}$ T cells), and $CD8^{+}$ T cells were sorted from PBMCs of healthy individuals using FACSAria Fusion (BD Biosciences). A total of 1×10^{5}

whole PBMCs or a total of 1×10^4 each sorted T cell subset in the presence of 1×10^5 irradiated APCs were stimulated with anti-CD3 mAb (clone: OKT3) and anti-CD28 mAb (clone: CD28.2) and cultured in glucose-free RPMI medium (Thermo Fisher Scientific) supplemented with 10% lipids without FBS (Biowest, Nuaillé, France), 10 IU/ml IL-2, 20 ng/ml IL-7, 1 mM glucose, and the indicated concentration of palmitate- or oleate-BSA.

PBMC co-culture with cancer cells

$MKN1^{WT}$ or $MKN1^{Y42C}$ cells were cultured for seven days in glucose-free RPMI medium (Thermo Fisher Scientific) supplemented with 10% lipid-without FBS (Biowest) under low-glucose (3 mM) condition. eTreg cells, conv $CD4^+$ T cells, and $CD8^+$ T cells were sorted from PBMCs of healthy individuals using FACSAria Fusion (BD Biosciences). A total of 1×10^4 sorted T cell subsets were stimulated with anti-CD3 mAb and anti-CD28 mAb and cultured with 1×10^5 irradiated APCs in the same wells of $MKN1^{WT}$ or $MKN1^{Y42C}$ cells, supplemented with 10 IU/ml IL-2 and 20 ng/ml IL-7, without contact with cancer cells.

Suppression assay

$CD45RA^-CD25^{high}CD4^+$ T cells (eTreg cells) were sorted from PBMCs using FACSAria Fusion (BD Biosciences). A total of 1×10^4 CFSE-labelled (1 μM) responder $CD8^+$ T cells (Tresp cells) from PBMCs or TILs were cocultured with/without unlabelled eTreg cells in the presence of 1×10^5

irradiated APCs and 0.5 μg/ml anti-CD3 mAb (clone: OKT3) under the indicated condition of culture medium. Proliferation was assessed four days later by dilution of CFSE-labelled cells with flow cytometry.

QUANTIFICATION AND STATISTICAL ANALYSIS

GraphPad Prism7 (GraphPad Software, San Diego, California, USA) or R version 3.1.1 (R Foundation for Statistical Computing, Vienna, Austria) was used for statistical analysis. The relations between groups were compared using a t-test or the nonparametric Mann-Whitney U test. The relations between tumor volume curves were compared using a two-way ANOVA test. Survival was analyzed by the Kaplan-Meier method and was compared with log-rank test. P values < 0.05 were considered statistically significant. For multiple testing, Bonferroni method was employed.

References

Ali, K., Soond, D.R., Pineiro, R., Hagemann, T., Pearce, W., Lim, E.L., Bouabe, H., Scudamore, C.L., Hancox, T., Maecker, H., *et al.* (2014). Inactivation of PI(3)K p110delta breaks regulatory T-cell-mediated immune tolerance to cancer. Nature *510*, 407-411.

Angelin, A., Gil-de-Gomez, L., Dahiya, S., Jiao, J., Guo, L., Levine, M.H., Wang, Z., Quinn, W.J., 3rd, Kopinski, P.K., Wang, L., *et al.* (2017). Foxp3 Reprograms T Cell Metabolism to Function in Low-Glucose, High-Lactate Environments. Cell metabolism *25*, 1282-1293.e1287.

Ayers, M., Lunceford, J., Nebozhyn, M., Murphy, E., Loboda, A., Kaufman, D.R., Albright, A., Cheng, J.D., Kang, S.P., Shankaran, V., *et al.* (2017). IFN-γ-related mRNA profile predicts clinical response to PD-1 blockade. The Journal of clinical investigation *127*, 2930-2940.

Bae, C.D., Min, D.S., Fleming, I.N., and Exton, J.H. (1998). Determination of interaction sites on the small G protein RhoA for phospholipase D. The Journal of biological chemistry *273*, 11596-11604.

Borghaei, H., Paz-Ares, L., Horn, L., Spigel, D.R., Steins, M., Ready, N.E., Chow, L.Q., Vokes, E.E., Felip, E., Holgado, E., *et al.* (2015). Nivolumab versus Docetaxel in Advanced Nonsquamous Non-Small-Cell Lung Cancer. The New England journal of medicine *373*, 1627-1639.

Cancer Genome Atlas Research Network. (2014). Comprehensive molecular characterization of gastric adenocarcinoma. Nature *513*, 202-209.

Chang, C.H., Qiu, J., O'Sullivan, D., Buck, M.D., Noguchi, T., Curtis, J.D., Chen, Q., Gindin, M., Gubin, M.M., van der Windt, G.J., *et al.* (2015). Metabolic Competition in the Tumor Microenvironment Is a Driver of Cancer Progression. Cell *162*, 1229-1241.

Cipolletta, D., Feuerer, M., Li, A., Kamei, N., Lee, J., Shoelson, S.E., Benoist, C., and Mathis, D. (2012). PPAR-gamma is a major driver of the accumulation and phenotype of adipose tissue Treg cells. Nature *486*, 549-553.

Curiel, T.J., Coukos, G., Zou, L., Alvarez, X., Cheng, P., Mottram, P., Evdemon-Hogan, M., Conejo-Garcia, J.R., Zhang, L., Burow, M., *et al.* (2004). Specific recruitment of regulatory T cells in ovarian carcinoma fosters immune privilege and predicts reduced survival. Nature medicine *10*, 942-949.

Currie, E., Schulze, A., Zechner, R., Walther, T.C., and Farese, R.V., Jr. (2013). Cellular fatty acid metabolism and cancer. Cell metabolism *18*, 153-161.

Duvel, K., Yecies, J.L., Menon, S., Raman, P., Lipovsky, A.I., Souza, A.L., Triantafellow, E., Ma, Q., Gorski, R., Cleaver, S., *et al.* (2010). Activation of a metabolic gene regulatory network downstream of mTOR complex 1. Molecular cell *39*, 171-183.

Fan, M.Y., and Turka, L.A. (2018). Immunometabolism and PI(3)K Signaling As a Link between IL-2, Foxp3 Expression, and Suppressor Function in Regulatory T Cells. Frontiers in immunology *9*, 69.

Fridman, W.H., Pages, F., Sautes-Fridman, C., and Galon, J. (2012). The immune contexture in human tumours: impact on clinical outcome. Nature reviews. Cancer *12*, 298-306.

Fruman, D.A., Chiu, H., Hopkins, B.D., Bagrodia, S., Cantley, L.C., and Abraham, R.T. (2017). The PI3K Pathway in Human Disease. Cell *170*, 605-635.

Gatenby, R.A., and Gillies, R.J. (2004). Why do cancers have high aerobic glycolysis? Nature reviews. Cancer *4*,

891-899.
Gerriets, V.A., Kishton, R.J., Johnson, M.O., Cohen, S., Siska, P.J., Nichols, A.G., Warmoes, M.O., de Cubas, A.A., MacIver, N.J., Locasale, J.W.*, et al.* (2016). Foxp3 and Toll-like receptor signaling balance Treg cell anabolic metabolism for suppression. Nature immunology *17*, 1459-1466.
Gorbachev, A.V., Kobayashi, H., Kudo, D., Tannenbaum, C.S., Finke, J.H., Shu, S., Farber, J.M., and Fairchild, R.L. (2007). CXC chemokine ligand 9/monokine induced by IFN-gamma production by tumor cells is critical for T cell-mediated suppression of cutaneous tumors. Journal of immunology (Baltimore, Md. : 1950) *178*, 2278-2286.
Gouw, A.M., Eberlin, L.S., Margulis, K., Sullivan, D.K., Toal, G.G., Tong, L., Zare, R.N., and Felsher, D.W. (2017). Oncogene KRAS activates fatty acid synthase, resulting in specific ERK and lipid signatures associated with lung adenocarcinoma. Proceedings of the National Academy of Sciences of the United States of America *114*, 4300-4305.
Griffith, J.W., Sokol, C.L., and Luster, A.D. (2014). Chemokines and chemokine receptors: positioning cells for host defense and immunity. Annual review of immunology *32*, 659-702.
Harikumar, K.B., Yester, J.W., Surace, M.J., Oyeniran, C., Price, M.M., Huang, W.C., Hait, N.C., Allegood, J.C., Yamada, A., Kong, X.*, et al.* (2014). K63-linked polyubiquitination of transcription factor IRF1 is essential for IL-1-induced production of chemokines CXCL10 and CCL5. Nature immunology *15*, 231-238.
Hensbergen, P.J., Wijnands, P.G., Schreurs, M.W., Scheper, R.J., Willemze, R., and Tensen, C.P. (2005). The CXCR3 targeting chemokine CXCL11 has potent antitumor activity in vivo involving attraction of CD8+ T lymphocytes but not inhibition of angiogenesis. Journal of immunotherapy (Hagerstown, Md. : 1997) *28*, 343-351.
Ho, P.C., and Kaech, S.M. (2017). Reenergizing T cell anti-tumor immunity by harnessing immunometabolic checkpoints and machineries. Current opinion in immunology *46*, 38-44.
Hoelzinger, D.B., Smith, S.E., Mirza, N., Dominguez, A.L., Manrique, S.Z., and Lustgarten, J. (2010). Blockade of CCL1 inhibits T regulatory cell suppressive function enhancing tumor immunity without affecting T effector responses. Journal of immunology (Baltimore, Md. : 1950) *184*, 6833-6842.
Janku, F., Yap, T.A., and Meric-Bernstam, F. (2018). Targeting the PI3K pathway in cancer: are we making headway? Nature reviews. Clinical oncology *15*, 273-291.
Jia, S., Liu, Z., Zhang, S., Liu, P., Zhang, L., Lee, S.H., Zhang, J., Signoretti, S., Loda, M., Roberts, T.M., and Zhao, J.J. (2008). Essential roles of PI(3)K-p110beta in cell growth, metabolism and tumorigenesis. Nature *454*, 776-779.
Jiang, H., Hegde, S., Knolhoff, B.L., Zhu, Y., Herndon, J.M., Meyer, M.A., Nywening, T.M., Hawkins, W.G., Shapiro, I.M., Weaver, D.T.*, et al.* (2016). Targeting focal adhesion kinase renders pancreatic cancers responsive to checkpoint immunotherapy. Nature medicine *22*, 851-860.
Kakiuchi, M., Nishizawa, T., Ueda, H., Gotoh, K., Tanaka, A., Hayashi, A., Yamamoto, S., Tatsuno, K., Katoh, H., Watanabe, Y.*, et al.* (2014). Recurrent gain-of-function mutations of RHOA in diffuse-type gastric carcinoma. Nature genetics *46*, 583-587.
Kamada, T., Togashi, Y., Tay, C., Ha, D., Sasaki, A., Nakamura, Y., Sato, E., Fukuoka, S., Tada, Y., Tanaka, A.,

et al. (2019). PD-1(+) regulatory T cells amplified by PD-1 blockade promote hyperprogression of cancer. Proceedings of the National Academy of Sciences of the United States of America.

Kang, Y.K., Boku, N., Satoh, T., Ryu, M.H., Chao, Y., Kato, K., Chung, H.C., Chen, J.S., Muro, K., Kang, W.K., *et al.* (2017). Nivolumab in patients with advanced gastric or gastro-oesophageal junction cancer refractory to, or intolerant of, at least two previous chemotherapy regimens (ONO-4538-12, ATTRACTION-2): a randomised, double-blind, placebo-controlled, phase 3 trial. Lancet (London, England) *390*, 2461-2471.

Kim, D., Pertea, G., Trapnell, C., Pimentel, H., Kelley, R., and Salzberg, S.L. (2013). TopHat2: accurate alignment of transcriptomes in the presence of insertions, deletions and gene fusions. Genome biology *14*, R36.

Kishore, M., Cheung, K.C.P., Fu, H., Bonacina, F., Wang, G., Coe, D., Ward, E.J., Colamatteo, A., Jangani, M., Baragetti, A., *et al.* (2017). Regulatory T Cell Migration Is Dependent on Glucokinase-Mediated Glycolysis. Immunity *47*, 875-889.e810.

Li, H., and Durbin, R. (2009). Fast and accurate short read alignment with Burrows-Wheeler transform. Bioinformatics *25*, 1754-1760.

Li, L., Liu, X., Sanders, K.L., Edwards, J.L., Ye, J., Si, F., Gao, A., Huang, L., Hsueh, E.C., Ford, D.A., *et al.* (2019). TLR8-Mediated Metabolic Control of Human Treg Function: A Mechanistic Target for Cancer Immunotherapy. Cell metabolism *29*, 103-123.e105.

Macintyre, A.N., Finlay, D., Preston, G., Sinclair, L.V., Waugh, C.M., Tamas, P., Feijoo, C., Okkenhaug, K., and Cantrell, D.A. (2011). Protein kinase B controls transcriptional programs that direct cytotoxic T cell fate but is dispensable for T cell metabolism. Immunity *34*, 224-236.

Maeda, Y., Nishikawa, H., Sugiyama, D., Ha, D., Hamaguchi, M., Saito, T., Nishioka, M., Wing, J.B., Adeegbe, D., Katayama, I., and Sakaguchi, S. (2014). Detection of self-reactive CD8(+) T cells with an anergic phenotype in healthy individuals. Science *346*, 1536-1540.

Mantovani, A., Marchesi, F., Malesci, A., Laghi, L., and Allavena, P. (2017). Tumour-associated macrophages as treatment targets in oncology. Nature reviews. Clinical oncology *14*, 399-416.

Michalek, R.D., Gerriets, V.A., Jacobs, S.R., Macintyre, A.N., MacIver, N.J., Mason, E.F., Sullivan, S.A., Nichols, A.G., and Rathmell, J.C. (2011). Cutting edge: distinct glycolytic and lipid oxidative metabolic programs are essential for effector and regulatory CD4+ T cell subsets. Journal of immunology (Baltimore, Md. : 1950) *186*, 3299-3303.

Miyara, M., Yoshioka, Y., Kitoh, A., Shima, T., Wing, K., Niwa, A., Parizot, C., Taflin, C., Heike, T., Valeyre, D., *et al.* (2009). Functional delineation and differentiation dynamics of human CD4+ T cells expressing the FoxP3 transcription factor. Immunity *30*, 899-911.

Muraoka, D., Kato, T., Wang, L., Maeda, Y., Noguchi, T., Harada, N., Takeda, K., Yagita, H., Guillaume, P., Luescher, I., *et al.* (2010). Peptide vaccine induces enhanced tumor growth associated with apoptosis induction in CD8+ T cells. Journal of immunology (Baltimore, Md. : 1950) *185*, 3768-3776.

Muroski, M.E., Miska, J., Chang, A.L., Zhang, P., Rashidi, A., Moore, H., Lopez-Rosas, A., Han, Y., and Lesniak, M.S. (2017). Fatty Acid Uptake in T Cell Subsets Using a Quantum Dot Fatty Acid Conjugate. Sci Rep *7*, 5790.

Nagarsheth, N., Wicha, M.S., and Zou, W. (2017). Chemokines in the cancer microenvironment and their relevance in cancer immunotherapy. Nature reviews. Immunology *17*, 559-572.

Okkenhaug, K., Patton, D.T., Bilancio, A., Garcon, F., Rowan, W.C., and Vanhaesebroeck, B. (2006). The p110delta isoform of phosphoinositide 3-kinase controls clonal expansion and differentiation of Th cells. Journal of immunology (Baltimore, Md. : 1950) *177*, 5122-5128.

Patton, D.T., Garden, O.A., Pearce, W.P., Clough, L.E., Monk, C.R., Leung, E., Rowan, W.C., Sancho, S., Walker, L.S., Vanhaesebroeck, B., and Okkenhaug, K. (2006). Cutting edge: the phosphoinositide 3-kinase p110 delta is critical for the function of CD4+CD25+Foxp3+ regulatory T cells. Journal of immunology (Baltimore, Md. : 1950) *177*, 6598-6602.

Peng, W., Chen, J.Q., Liu, C., Malu, S., Creasy, C., Tetzlaff, M.T., Xu, C., McKenzie, J.A., Zhang, C., Liang, X.*, et al.* (2016). Loss of PTEN Promotes Resistance to T Cell-Mediated Immunotherapy. Cancer discovery *6*, 202-216.

Peterson, T.R., Sengupta, S.S., Harris, T.E., Carmack, A.E., Kang, S.A., Balderas, E., Guertin, D.A., Madden, K.L., Carpenter, A.E., Finck, B.N., and Sabatini, D.M. (2011). mTOR complex 1 regulates lipin 1 localization to control the SREBP pathway. Cell *146*, 408-420.

Porstmann, T., Santos, C.R., Griffiths, B., Cully, M., Wu, M., Leevers, S., Griffiths, J.R., Chung, Y.L., and Schulze, A. (2008). SREBP activity is regulated by mTORC1 and contributes to Akt-dependent cell growth. Cell metabolism *8*, 224-236.

Procaccini, C., Carbone, F., Di Silvestre, D., Brambilla, F., De Rosa, V., Galgani, M., Faicchia, D., Marone, G., Tramontano, D., Corona, M.*, et al.* (2016). The Proteomic Landscape of Human Ex Vivo Regulatory and Conventional T Cells Reveals Specific Metabolic Requirements. Immunity *44*, 406-421.

Qureshi, O.S., Zheng, Y., Nakamura, K., Attridge, K., Manzotti, C., Schmidt, E.M., Baker, J., Jeffery, L.E., Kaur, S., Briggs, Z.*, et al.* (2011). Trans-endocytosis of CD80 and CD86: a molecular basis for the cell-extrinsic function of CTLA-4. Science *332*, 600-603.

Ramana, C.V., Chatterjee-Kishore, M., Nguyen, H., and Stark, G.R. (2000). Complex roles of Stat1 in regulating gene expression. Oncogene *19*, 2619-2627.

Reck, M., Rodríguez-Abreu, D., Robinson, A.G., Hui, R., Csőszi, T., Fülöp, A., Gottfried, M., Peled, N., Tafreshi, A., Cuffe, S.*, et al.* (2016). Pembrolizumab versus Chemotherapy for PD-L1-Positive Non-Small-Cell Lung Cancer. The New England journal of medicine *375*, 1823-1833.

Rizvi, N.A., Hellmann, M.D., Snyder, A., Kvistborg, P., Makarov, V., Havel, J.J., Lee, W., Yuan, J., Wong, P., Ho, T.S.*, et al.* (2015). Cancer immunology. Mutational landscape determines sensitivity to PD-1 blockade in non-small cell lung cancer. Science *348*, 124-128.

Robert, C., Schachter, J., Long, G.V., Arance, A., Grob, J.J., Mortier, L., Daud, A., Carlino, M.S., McNeil, C., Lotem, M.*, et al.* (2015). Pembrolizumab versus Ipilimumab in Advanced Melanoma. The New England journal of medicine *372*, 2521-2532.

Rohrig, F., and Schulze, A. (2016). The multifaceted roles of fatty acid synthesis in cancer. Nature reviews. Cancer *16*, 732-749.

Rooney, M.S., Shukla, S.A., Wu, C.J., Getz, G., and Hacohen, N. (2015). Molecular and genetic properties of tumors associated with local immune cytolytic activity. Cell *160*, 48-61.

Sahai, E., Alberts, A.S., and Treisman, R. (1998). RhoA effector mutants reveal distinct effector pathways for

cytoskeletal reorganization, SRF activation and transformation. The EMBO journal *17*, 1350-1361.

Saito, T., Nishikawa, H., Wada, H., Nagano, Y., Sugiyama, D., Atarashi, K., Maeda, Y., Hamaguchi, M., Ohkura, N., Sato, E.*, et al.* (2016). Two FOXP3(+)CD4(+) T cell subpopulations distinctly control the prognosis of colorectal cancers. Nature medicine *22*, 679-684.

Sato, E., Olson, S.H., Ahn, J., Bundy, B., Nishikawa, H., Qian, F., Jungbluth, A.A., Frosina, D., Gnjatic, S., Ambrosone, C.*, et al.* (2005). Intraepithelial CD8+ tumor-infiltrating lymphocytes and a high CD8+/regulatory T cell ratio are associated with favorable prognosis in ovarian cancer. Proceedings of the National Academy of Sciences of the United States of America *102*, 18538-18543.

Sauer, S., Bruno, L., Hertweck, A., Finlay, D., Leleu, M., Spivakov, M., Knight, Z.A., Cobb, B.S., Cantrell, D., O'Connor, E.*, et al.* (2008). T cell receptor signaling controls Foxp3 expression via PI3K, Akt, and mTOR. Proceedings of the National Academy of Sciences of the United States of America *105*, 7797-7802.

Schachter, J., Ribas, A., Long, G.V., Arance, A., Grob, J.J., Mortier, L., Daud, A., Carlino, M.S., McNeil, C., Lotem, M.*, et al.* (2017). Pembrolizumab versus ipilimumab for advanced melanoma: final overall survival results of a multicentre, randomised, open-label phase 3 study (KEYNOTE-006). Lancet (London, England) *390*, 1853-1862.

Selby, M.J., Engelhardt, J.J., Quigley, M., Henning, K.A., Chen, T., Srinivasan, M., and Korman, A.J. (2013). Anti-CTLA-4 antibodies of IgG2a isotype enhance antitumor activity through reduction of intratumoral regulatory T cells. Cancer immunology research *1*, 32-42.

Shitara, K., Özgüroğlu, M., Bang, Y.J., Di Bartolomeo, M., Mandalà, M., Ryu, M.H., Fornaro, L., Olesiński, T., Caglevic, C., Chung, H.C.*, et al.* (2018). Pembrolizumab versus paclitaxel for previously treated, advanced gastric or gastro-oesophageal junction cancer (KEYNOTE-061): a randomised, open-label, controlled, phase 3 trial. Lancet (London, England) *392*, 123-133.

Simpson, T.R., Li, F., Montalvo-Ortiz, W., Sepulveda, M.A., Bergerhoff, K., Arce, F., Roddie, C., Henry, J.Y., Yagita, H., Wolchok, J.D.*, et al.* (2013). Fc-dependent depletion of tumor-infiltrating regulatory T cells co-defines the efficacy of anti-CTLA-4 therapy against melanoma. J Exp Med *210*, 1695-1710.

Soond, D.R., Bjorgo, E., Moltu, K., Dale, V.Q., Patton, D.T., Torgersen, K.M., Galleway, F., Twomey, B., Clark, J., Gaston, J.S.*, et al.* (2010). PI3K p110delta regulates T-cell cytokine production during primary and secondary immune responses in mice and humans. Blood *115*, 2203-2213.

Spranger, S., Bao, R., and Gajewski, T.F. (2015). Melanoma-intrinsic beta-catenin signalling prevents anti-tumour immunity. Nature *523*, 231-235.

Spranger, S., Spaapen, R.M., Zha, Y., Williams, J., Meng, Y., Ha, T.T., and Gajewski, T.F. (2013). Up-regulation of PD-L1, IDO, and T(regs) in the melanoma tumor microenvironment is driven by CD8(+) T cells. Science translational medicine *5*, 200ra116.

Subramanian, A., Tamayo, P., Mootha, V.K., Mukherjee, S., Ebert, B.L., Gillette, M.A., Paulovich, A., Pomeroy, S.L., Golub, T.R., Lander, E.S., and Mesirov, J.P. (2005). Gene set enrichment analysis: a knowledge-based approach for interpreting genome-wide expression profiles. Proceedings of the National Academy of Sciences of the United States of America *102*, 15545-15550.

Sugiyama, E., Togashi, Y., Takeuchi, Y., Shinya, S., Tada, Y., Kataoka, K., Tane, K., Sato, E., Ishii, G., Goto, K.,

et al. (2020). Blockade of EGFR improves responsiveness to PD-1 blockade in EGFR-mutated non-small cell lung cancer. Science immunology *5*.

Tada, Y., Togashi, Y., Kotani, D., Kuwata, T., Sato, E., Kawazoe, A., Doi, T., Wada, H., Nishikawa, H., and Shitara, K. (2018). Targeting VEGFR2 with Ramucirumab strongly impacts effector/ activated regulatory T cells and CD8(+) T cells in the tumor microenvironment. Journal for immunotherapy of cancer *6*, 106.

Takeuchi, Y., Tanemura, A., Tada, Y., Katayama, I., Kumanogoh, A., and Nishikawa, H. (2018). Clinical response to PD-1 blockade correlates with a sub-fraction of peripheral central memory CD4+ T cells in patients with malignant melanoma. International immunology *30*, 13-22.

Togashi, Y., Shitara, K., and Nishikawa, H. (2019). Regulatory T cells in cancer immunosuppression - implications for anticancer therapy. Nature reviews. Clinical oncology.

Tran, D.Q., Ramsey, H., and Shevach, E.M. (2007). Induction of FOXP3 expression in naive human CD4+FOXP3 T cells by T-cell receptor stimulation is transforming growth factor-beta dependent but does not confer a regulatory phenotype. Blood *110*, 2983-2990.

Trapnell, C., Roberts, A., Goff, L., Pertea, G., Kim, D., Kelley, D.R., Pimentel, H., Salzberg, S.L., Rinn, J.L., and Pachter, L. (2012). Differential gene and transcript expression analysis of RNA-seq experiments with TopHat and Cufflinks. Nature protocols *7*, 562-578.

Tsai, C.C., Kai, J.I., Huang, W.C., Wang, C.Y., Wang, Y., Chen, C.L., Fang, Y.T., Lin, Y.S., Anderson, R., Chen, S.H.*, et al.* (2009). Glycogen synthase kinase-3beta facilitates IFN-gamma-induced STAT1 activation by regulating Src homology-2 domain-containing phosphatase 2. Journal of immunology (Baltimore, Md. : 1950) *183*, 856-864.

Van Raemdonck, K., Van den Steen, P.E., Liekens, S., Van Damme, J., and Struyf, S. (2015). CXCR3 ligands in disease and therapy. Cytokine & growth factor reviews *26*, 311-327.

Wakil, S.J. (1989). Fatty acid synthase, a proficient multifunctional enzyme. Biochemistry *28*, 4523-4530.

Wang, H., Franco, F., and Ho, P.C. (2017). Metabolic Regulation of Tregs in Cancer: Opportunities for Immunotherapy. Trends in cancer *3*, 583-592.

Wang, K., Yuen, S.T., Xu, J., Lee, S.P., Yan, H.H., Shi, S.T., Siu, H.C., Deng, S., Chu, K.M., Law, S.*, et al.* (2014). Whole-genome sequencing and comprehensive molecular profiling identify new driver mutations in gastric cancer. Nature genetics *46*, 573-582.

Warburg, O. (1956). On the origin of cancer cells. Science *123*, 309-314.

Weber, J.S., D'Angelo, S.P., Minor, D., Hodi, F.S., Gutzmer, R., Neyns, B., Hoeller, C., Khushalani, N.I., Miller, W.H., Jr., Lao, C.D.*, et al.* (2015). Nivolumab versus chemotherapy in patients with advanced melanoma who progressed after anti-CTLA-4 treatment (CheckMate 037): a randomised, controlled, open-label, phase 3 trial. The Lancet. Oncology *16*, 375-384.

Weinberg, S.E., Singer, B.D., Steinert, E.M., Martinez, C.A., Mehta, M.M., Martinez-Reyes, I., Gao, P., Helmin, K.A., Abdala-Valencia, H., Sena, L.A.*, et al.* (2019). Mitochondrial complex III is essential for suppressive function of regulatory T cells. Nature *565*, 495-499.

Wiig, H., Aukland, K., and Tenstad, O. (2003). Isolation of interstitial fluid from rat mammary tumors by a centrifugation method. American journal of physiology. Heart and circulatory physiology *284*, H416-424.

Wing, K., Onishi, Y., Prieto-Martin, P., Yamaguchi, T., Miyara, M., Fehervari, Z., Nomura, T., and Sakaguchi, S. (2008). CTLA-4 control over Foxp3+ regulatory T cell function. Science *322*, 271-275.

Yamamoto, M., Nomura, S., Hosoi, A., Nagaoka, K., Iino, T., Yasuda, T., Saito, T., Matsushita, H., Uchida, E., Seto, Y.*, et al.* (2018). Established gastric cancer cell lines transplantable into C57BL/6 mice show fibroblast growth factor receptor 4 promotion of tumor growth. Cancer science *109*, 1480-1492.

Yang, C.H., Wei, L., Pfeffer, S.R., Du, Z., Murti, A., Valentine, W.J., Zheng, Y., and Pfeffer, L.M. (2007). Identification of CXCL11 as a STAT3-dependent gene induced by IFN. Journal of immunology (Baltimore, Md. : 1950) *178*, 986-992.

Yoo, H.Y., Sung, M.K., Lee, S.H., Kim, S., Lee, H., Park, S., Kim, S.C., Lee, B., Rho, K., Lee, J.E.*, et al.* (2014). A recurrent inactivating mutation in RHOA GTPase in angioimmunoblastic T cell lymphoma. Nature genetics *46*, 371-375.

Zumwalt, T.J., Arnold, M., Goel, A., and Boland, C.R. (2015). Active secretion of CXCL10 and CCL5 from colorectal cancer microenvironments associates with GranzymeB+ CD8+ T-cell infiltration. Oncotarget *6*, 2981-2991.